GEOPHYSICS, VOL. 77, NO. 4 (JULY-AUGUST 2012); P. E281–E299, 21 FIGS., 4 TABLES.
10.1190/GEO2011-0380.1

Marine CSEM of the Scarborough gas field, Part 1: Experimental design and data uncertainty

David Myer[1], Steven Constable[2], Kerry Key[2], Michael E. Glinsky[3], and Guimin Liu[4]

ABSTRACT

We describe the planning, processing, and uncertainty analysis for a marine CSEM survey of the Scarborough gas field off the northwest coast of Australia, consisting of 20 transmitter tow lines and 144 deployments positioned along a dense 2D profile and a complex 3D grid. The purpose of this survey was to collect a high-quality data set over a known hydrocarbon prospect and use it to further the development of CSEM as a hydrocarbon mapping tool. Recent improvements in navigation and processing techniques yielded high-quality frequency domain data. Data pseudosections exhibit a significant anomaly that is laterally confined within the known reservoir location. Perturbation analysis of the uncertainties in the transmitter parameters yielded predicted uncertainties in amplitude and phase of just a few percent at close ranges. These uncertainties may, however, be underestimated. We introduce a method for more accurately deriving uncertainties using a line of receivers towed twice in opposite directions. Comparing the residuals for each line yields a Gaussian distribution directly related to the aggregate uncertainty of the transmitter parameters. Constraints on systematic error in the transmitter antenna dip and inline range can be calculated by perturbation analysis. Uncertainties are not equal in amplitude and phase, suggesting that inversion of these data would be better suited in these components rather than in real and imaginary components. One-dimensional inversion showed that the reservoir and a confounding resistive layer above it cannot be separately resolved even when the roughness constraint is modified to allow for jumps in resistivity and prejudices are provided, indicating that this level of detail is beyond the single-site CSEM data. Further, when range-dependent error bars are used, the resolution decreases at a shallower depth than when a fixed-error level is used.

INTRODUCTION

The marine controlled-source electromagnetic method (CSEM) uses an electric current dipole to create a source field that is measured at receivers placed across the seafloor. The electric field diffuses through the earth and contains information about the electrical conductivity of the seabed. Electrical conductivity in sedimentary sections is largely controlled by the porosity and composition of pore fluids within the sediments. Though the resolution is not as fine-scaled as the wave-propagation of seismics, CSEM surveying is more detailed than a potential field method like gravity (Cox et al., 1986; Constable and Cox, 1996; MacGregor et al., 2001; Edwards, 2005). Over the past decade, there has been increasing interest in the use of CSEM for hydrocarbon exploration because of its sensitivity to thin resistive layers embedded in conductive strata. (For recent reviews, see Constable [2010], Zhdanov [2010], and Key [2011].) The race to commercialization often has been leveraged by the use of academically designed equipment such as the Scripps ocean bottom electromagnetic instrument (OBEM) (Webb et al., 1985; Constable et al., 1998) and the Southampton deep-towed active source instrument (Sinha et al., 1990). Although some limited data has been made available to academic researchers (e.g., Newman et al., 2010), the research community has lacked general access to a data set with which to further our understanding of the

Manuscript received by the Editor 4 October 2011; revised manuscript received 2 February 2012; published online 27 June 2012.
[1]University of California at San Diego, Scripps Institution of Oceanography, La Jolla, California, USA and BlueGreen Geophysics, LLC, Encinitas, California, USA. E-mail: dmyer@bluegreengeophysics.com.
[2]University of California at San Diego, Scripps Institution of Oceanography, La Jolla, California, USA. E-mail: sconstable@ucsd.edu; kkey@ucsd.edu.
[3]CSIRO Earth Science and Resource Engineering, Kensington, Australia and University of Western Australia, School of Physics, Crawley, Australia. E-mail: michael.glinsky@csiro.au.
[4]BHP Billiton, Resource Assessment R&D, Melbourne, Australia. E-mail: guimin.liu@bhpbilliton.com.

method. We had the opportunity to remedy this situation by carrying out a comprehensive electromagnetic survey in 2009 over the Scarborough gas reservoir on the Exmouth Plateau, off the northwest shelf of Australia (Figure 1).

The Scarborough survey was designed to cover a wide range of geometries and data types to demonstrate the effectiveness of marine EM methods for hydrocarbon exploration and to allow for the development and testing of more complex interpretation methods. It was specifically designed to (1) obtain a calibration data set over a known structure with control from five wells and excellent 3D seismic data coverage to develop our ability to interpret data with 1D, 2D, and 3D forward and inverse modeling tools; (2) collect a data set suitable for joint magnetotelluric, CSEM, and seismic interpretation; (3) investigate the effect of shallow, confounding resistors; (4) understand how to optimize the density and geometry of CSEM receivers and transmitter tows; (5) examine how well CSEM data can differentiate between various reservoir thicknesses and saturations; and (6) examine noise and repeatability in CSEM data collection.

This survey also provided the opportunity to test a considerable number of instrument developments that had been made since our first hydrocarbon survey carried out in 2000 and reported by Ellingsrud et al. (2002). The receivers themselves were considerably improved over the four-channel, 16-bit instrument described by Constable et al. (1998). All included 24-bit digitization and 80% of the receivers used a more modern logging system with up to eight channels of data, allowing the installation of vertical electric field sensors in addition to the standard horizontal electric and magnetic field sensors. The smaller least count of the 24-bit system increased the dynamic range of the data and allowed us to reduce the gain from 1,000,000 to 10,000, reducing the effects of saturation when the transmitter was near the receivers. The large, front-end coupling capacitors were removed from the electric field amplifiers, which allowed more precise calibrations to be made. Orientations were recorded using external electronic compasses that were mounted as far from the distorting effects of magnetometers and batteries as possible. The seafloor receivers were supplemented by two instruments having twin 100 m antennas configured as gradiometers, to provide increased sensitivity and direct measurements of apparent phase velocity. A three-axis electric field instrument was towed at a fixed offset of a few hundred meters behind the transmitter to record near-surface variations in conductivity. Our newly developed transmitter was powered by a 400 Hz source in which every cycle was locked to GPS time, producing highly accurate phase data, and included a number of improvements to aid in navigation. The most innovative of these was an inverted long-baseline acoustic ranging system that used transponders towed behind the research vessel. The CSEM waveform had a usable bandwidth that was considerably larger than the traditional square wave, yet remained compact enough to carry out signal processing and noise estimation using recently developed prewhitening and stacking algorithms. The performance of many of these improvements are discussed in more detail below.

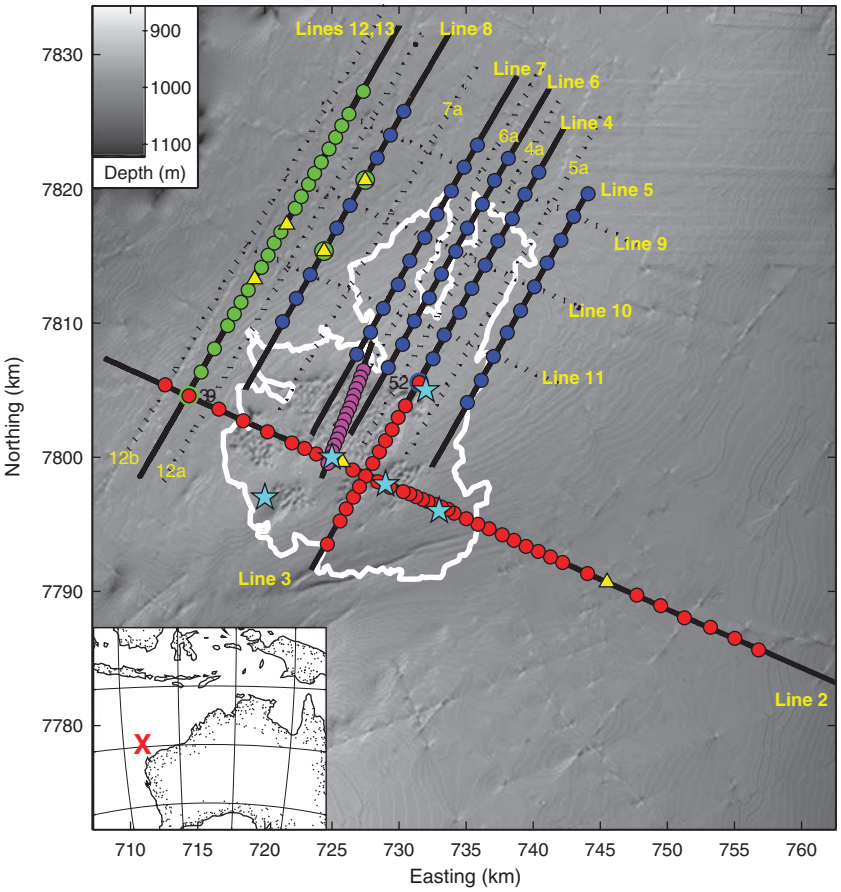

Figure 1. A bathymetric map overlain with the Scarborough instrument deployment locations (filled circles), predicted reservoir outline (white), exploration wells (stars), and tow lines (black lines). The inset shows the survey location off the west coast of Australia. LEMs are shown as yellow triangles. Phases 1–4 are colored red, blue, green, and magenta, respectively. Repeated deployments are shown with two colors. The two LEMs in phase two were replaced with OBEMs in phase three. The primary tow lines are solid lines, secondary tow lines are dotted.

In this paper, we present a review of the design, collection, and processing of this data set, as well as a detailed error analysis of the inline electric field data, arranged into the following sections. First, we present an overview of the survey area along with presurvey 1D modeling to highlight some of the challenges. This is followed by a review of the collection and processing of the CSEM data and a qualitative comparison of the data pseudosections with the expected results from modeling. In the "Error Analysis" section, we give a detailed analysis of the sources of uncertainty and translate them into a minimum error structure suitable for inversion.

SURVEY DESIGN

Scarborough gas field description

The Exmouth plateau (Figure 1) is a passive margin between continental and oceanic crust left over from the break-up of Australia and India, and is surrounded on three sides by oceanic crust at abyssal depths. The plateau, which is $\sim 400 \times 600$ km, is bounded to the northeast and southwest by transform faults. The transition between continental and oceanic crust to the

northwest is thought to be bounded by a subhorizontal detachment fault that undercuts the plateau at about 10 km depth, dipping toward the Australian continent (Driscoll and Karner, 1998). Since the Mesozoic era, the plateau has undergone a complex sequence of fracture, extension, uplift, truncation, and subsidence (Exon et al., 1982; Mutter and Larson, 1989; Lorenzo et al., 1991). The result is that the plateau is covered by a number of mostly horizontal sedimentary layers of resistivities varying between 1 and 10 Ωm.

Five exploration wells have been drilled in the Scarborough gas field and their data, combined with 3D seismic coverage, were used to define the areal extent and section profile of the reservoir. The white contour in Figure 1 is the expected edge of the reservoir — the boundary within which the concentration of gas is expected to be higher than the concentration of water. The reservoir itself (Figure 2) is a 20–30 m layer residing between 1900 and 2000 m below sea level (mbsl) in about 900–950 m of water. It has a moderate resistivity of 25 Ωm and is overlain by several thin layers of lower gas saturation with resistivities of 5–10 Ωm. To first order, CSEM is more sensitive to the resistivity-thickness product (T) than resistivity alone (Constable and Weiss, 2006; Key, 2011). For the reservoir stack, T is ~1000 Ωm^2, which is less than a factor of 10 above the background value of about 150–200 Ωm^2. In general, T for hydrocarbon-saturated reservoirs varies between 10^2–10^5 Ωm^2 and therefore, the Scarborough reservoir is a relatively small target. Because it is considered economically viable, it is important to establish the conditions under which CSEM can distinguish a low-contrast body such as is found here from the background.

Scarborough presents an additional challenge to CSEM in the form of a confounding resistive layer in the overburden. The Gearle siltstone formation lies a few hundred meters above the reservoir, between 1650 and 1750 mbsl (Veevers and Johnstone, 1974). Its resistivity-thickness product (300 Ωm^2) is between that of the background and that of the reservoir, and we expect the galvanic and inductive response of this layer to somewhat obscure sensitivity to the reservoir below.

Presurvey modeling

To characterize the size of the anomaly we expect from Scarborough and to find a suitable frequency range for transmission, we modeled the predicted geology in 2D with and without the reservoir using the finite element code of Key and Ovall (2011). This code uses a parallel, goal-oriented adaptive method to iteratively refine the finite-element mesh, producing electromagnetic responses accurate to a user-specified error tolerance. Here, we set a tolerance of 1%. The model without the reservoir is the set of 1D layers shown in Figure 2. The reservoir model added a 30-m-thick trapezoid with a top width of 10 km, a bottom width of 15 km, and 25 Ωm resistivity, overlain by a 10 m × 15 km prism of 10 Ωm separated from the main reservoir by 10 m.

Figure 3 shows the difference at multiple frequencies between the two models for a site in the middle of the reservoir. The data for each frequency is excluded when the range reaches 10 km (i.e., the edge of the reservoir) or the amplitude falls below the typical instrument noise floor of $1e-15$ V/Am^2. The initial CSEM survey off Angola chose 0.25 Hz as the fundamental frequency (Ellingsrud et al., 2002) and we have used it here as our starting point. Our model predicts that this frequency is not particularly sensitive to the configuration of the Scarborough reservoir, producing less than a 20% anomaly in amplitude and 20° in phase. The sensitivity to the reservoir increases with frequency, producing large anomalies at the higher frequencies of 0.75 Hz and 1.75 Hz. However, the maximum acquisition ranges for these frequencies are more constrained due to the increase in attenuation with frequency. Thus, to acquire useful CSEM data, peak output current of the transmitter should be around 1 Hz.

To investigate the level of accuracy required to resolve the reservoir, we inverted frequencies 0.25, 0.75, and 1.75 Hz of the forward model data using a variety of realizations of Gaussian noise and the 1D Occam inversion code of Key (2009) specifying a first-difference regularization constraint (i.e., "smooth" inversion). Figure 4a shows the resulting inversion models. Between 10% and 15% noise, resolution decreases to the point that there is relatively little sensitivity to resistivity variations above the resistive basement. At the 5% noise level, there is increased resolution to the bottom of the reservoir, but the signals of the Gearle layer and the reservoir are not distinguishable. Decreasing the noise level to 1% (not shown) produces no significant change over the 5% model.

The scale of structures that can be resolved by the inversion are limited by the smoothness constraint. We tested whether this is responsible for the ambiguity in resolving the reservoir separately from the Gearle by removing the penalty above and below the model layers positioned at the depths of these two geologic layers. To counter the destabilization this introduces into the inversion, a preference penalty was added to the Gearle and reservoir layers for deviating from 3 and 2 Ωm, respectively. This, however, was insufficient guidance to allow separation of the two layers. Instead, the

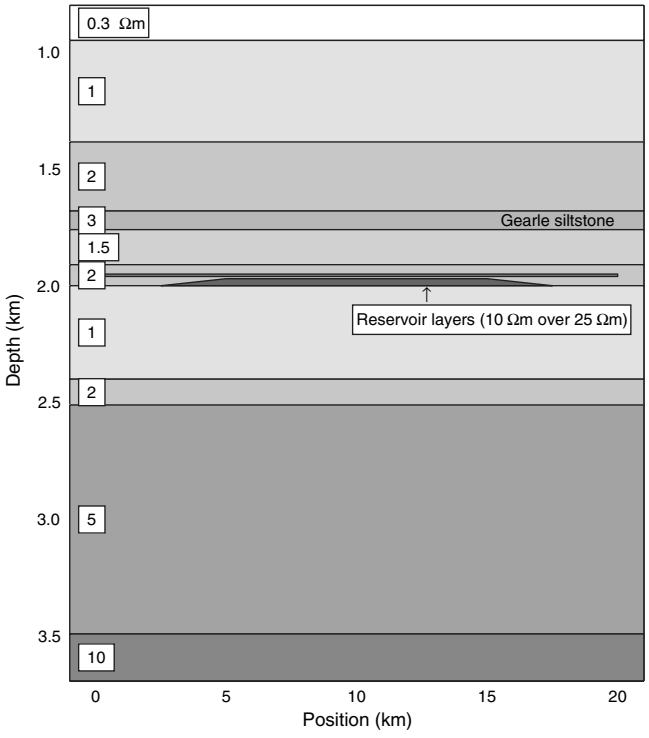

Figure 2. A simplified section view of the expected geologic background with resistivities for each layer. The reservoir is not a monolithic body, but a stack of thin traps ranging from 6 to 10 Ωm on top of a larger body of varying thickness and ~25 Ωm.

inversion created a large resistive layer between the Gearle and reservoir. We therefore increased the guidance given to the inversion by adding preference resistivities of 2, 1.5, and 1 Ωm for the geologic layers above the Gearle, between the Gearle and reservoir, and below the reservoir, respectively. We show in Figure 4b that with guidance constraints from the regional geology, the presence of separate layers can be determined even up to 20% noise, but that the magnitude of the reservoir declines with rising noise such that it might not be interpreted as a reservoir by the 15% noise level. Curiously, the Gearle layer is overestimated at all noise levels even though there is a penalty imposed whenever it varies from 3 Ωm. It is likely that the ~200 m spacing between the Gearle and Scarborough reservoir is too small for the diffusive CSEM method to resolve them separately. We expect that any inversion of the Scarborough data set will have a similar problem.

DATA

Data collection

We carried out the survey of the Scarborough gas field from 22 May through 23 June, 2009 from the UNOLS research vessel Roger Revelle. Using a fleet of 54 broadband EM receivers, we occupied 144 seafloor sites in four phases. In phase one, we deployed 40 sites southeast to northwest across the wide southern portion of the reservoir with site spacing varying from 2 km at the ends to 500 m in the middle. We also deployed a perpendicular line of 12 sites with a site spacing of 1–2 km. Forty of the instruments measured horizontal magnetic fields and three axes of electric fields, and ten measured only horizontal magnetic and electric fields. The remaining two sites were each deployed as single axis, long-wire EM (LEM) receivers (Webb et al., 1985) configured as gradiometers: two 100 m electrode pairs deployed in series. Sites in phase one remained on the seafloor between five and seven days, three days of which were devoted to towing our electric dipole source, the Scripps undersea electromagnetic source instrument (SUESI). On the remaining days, the instruments collected magnetotelluric data, which will be reported in a separate publication. The goal of phase one was to collect CSEM data over an area of essentially 1D structure.

SUESI was configured with a 250 m electric current dipole which was deep-towed 60 m above the seafloor at an average speed of 0.75 m/s (1.5 knots). It output 300 amps using the binary, broad-spectrum waveform "D" described in Myer et al. (2011). Because waveform D puts more power in the third, seventh, and 13th harmonics than the fundamental, we used a

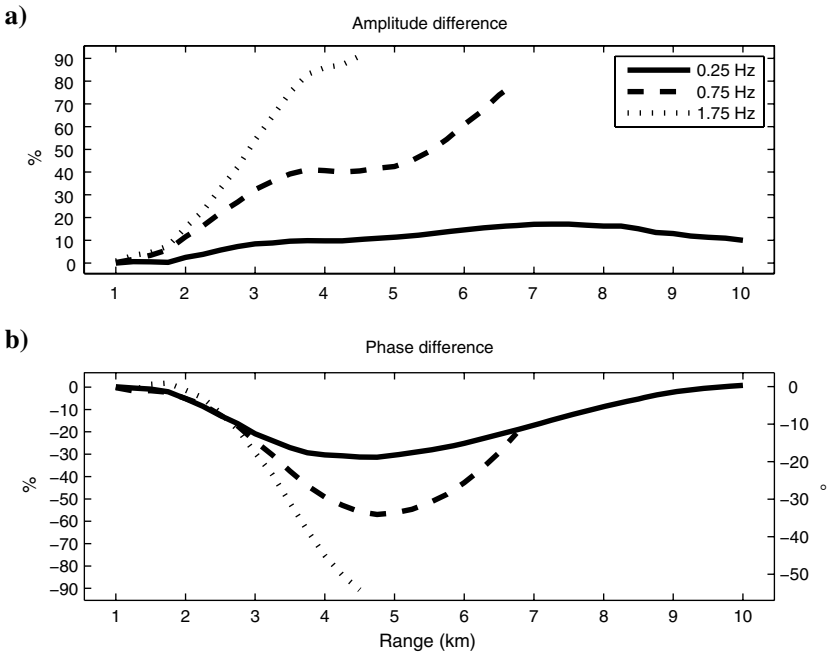

Figure 3. Difference between 2D models of the electric field (a) amplitudes and (b) phases with and without the Scarborough reservoir for a site positioned over the center of the reservoir. The model without the reservoir is the set of 1D layers shown in Figure 2. The reservoir model adds a 30-m-thick trapezoid with a top width of 10 km, a bottom width of 15 km and 25 Ωm resistivity, overlain by a 10 m × 15 km prism of 10 Ωm separated from the main reservoir by 10 m.

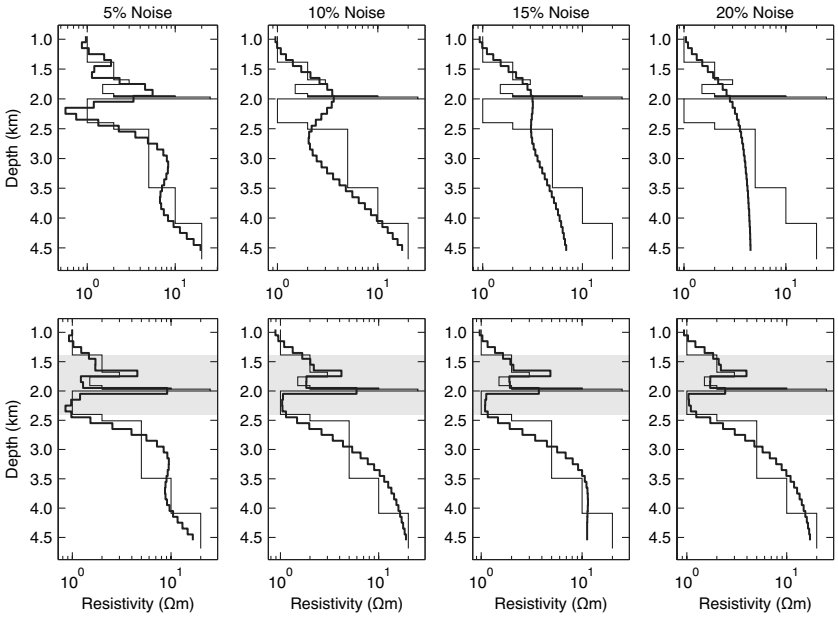

Figure 4. (top row) Models resulting from the 1D inversion of the 2D forward model on-reservoir data described in Figure 3 with different levels of Gaussian noise added. The thin black line is the forward model. The Gearle and reservoir layers cannot be distinguished separately with a smooth inversion and one needs less than 10% noise to image the bottom of the Gearle-reservoir complex. (bottom row) Models resulting from 1D inversion in which the roughness penalty has been removed above and below the Gearle and reservoir layers. To stabilize the inversions, a prejudice penalty for deviating from values of 2, 3, 1.5, 2, 1 Ωm is set for the five layers starting with the one above the Gearle, going to the one below the reservoir (demarcated by the grey area on the plot). Though the Gearle and reservoir can now be separated, the resistivity of the Gearle always is overestimated even though there is a penalty for doing so.

0.25 Hz waveform with peak output in the response frequencies of the reservoir: 0.75, 1.75, and 3.25 Hz. This also allowed us to test the prediction that 0.25 Hz would be relatively insensitive to the reservoir.

We towed the source over the long line twice and refer to these separate tows as lines one and two, although they cover the same receivers. The tow over the perpendicular line is referred to as "line three." During the line one tow, we configured and tested a new inverted long-baseline (iLBL) navigation system that uses acoustic ranging from a pair of surface-towed paravanes to triangulate the horizontal location of the transmitter vehicle (Key and Constable, manuscript in prep). Unfortunately, the iLBL system was not fully functional until after tow line one, so iLBL navigation solutions are only available for lines two and later. Because line two is a retow of line one in the opposite direction, we did not lose any data coverage of the reservoir.

SUESI is equipped with a Kongsberg Simrad 1007 altimeter and a Valeport Midas SVX2 CTDV (conductivity, temperature, depth, and sound velocity) sensor. These sensors provide, among other things, depth and altitude data, which are accurate to the submeter scale. The altimeter readout is continually monitored and digitally recorded so that the depth of the transmitter can be adjusted in real time to ensure that the desired tow height is maintained. A Paroscientific Inc. pressure sensor attached to the far electrode is used in the calculation of antenna dip. Additionally, we deployed an acoustic relay at the end of the antenna to be used in conjunction with the iLBL system to provide navigation of the antenna tail, but a fault in the relay transponder prevented it from functioning. The azimuth of the antenna will be discussed in more detail below.

We recovered all 52 instruments from phase one and redeployed 51 of them in phase two in a grid pattern of five lines over the northern portion of the reservoir (Figure 1). Receiver spacing along the lines is 2 km and the distance between the lines varies between 2 and 6 km. Two sites (51 and 52) from phase one were redeployed at the same locations for phase two to test the repeatability of CSEM results. Sites were deployed for between nine and 18 days, with longer deployments corresponding to sites which remained on the seafloor during phase three. The transmitter was towed continuously for six and a half days in twelve lines during this phase. Tow lines 4–8 are directly over the lines of receivers. Tow lines 4a–7a run between the lines of receivers and tow lines 9–11 run perpendicular. The goal of this phase was to collect a 3D data set with a large volume of broadside data and crossing lines over a morphologically complex body. The geologic model as reflected in the outline in Figure 1 indicates that the reservoir, which resides in the distal end of a turbidite fan (Boyd et al., 1992; Haq et al., 1992), splits into two parallel lobes like rabbit ears.

For phase three, we recovered and redeployed the two LEMs and 23 of the OBEMs from the eastern portion of phase two. Site 39 from phase one was reoccupied and the sites of the two LEMs from line eight of phase two were redeployed with OBEMs. The bulk of the instruments were deployed in a single line with 1 or 2 km spacing and the line was towed four times: once in each direction (lines 12 and 13), and broadside on either side (12a and 12b). Instruments were deployed for ~5 days with two and a half days occupied by towing of the source. At the end of phase three, all instruments were recovered.

Phase four targeted an area of possible hydrates located in the main body of the reservoir and denoted by pock-marks in the bathymetry. Because hydrates are generally shallow, the deep penetration of lower frequencies was not desired, so the fundamental frequency of the transmitter was moved upward to 0.5 Hz and the source dipole was shortened to 50 m. Also, the recording frequency of the receivers was increased from 62.5 Hz to 250 Hz. Sixteen instruments were deployed for less than a day each on a site spacing of 500 m and line 14 was towed directly over them. All equipment was recovered successfully.

For all four phases of this survey, an experimental three-axis towed electric-field receiver (Vulcan) was tethered 250 m beyond the end of the far electrode of the transmitter (Myer et al., 2010). For phases one through three, this placed the Vulcan 390 m from the center of the transmitter dipole. In phase four, in which a shorter dipole was used, a second Vulcan was added 250 m beyond the first. They were 280 m and 530 m from the center of the transmitter dipole, respectively.

Time series processing

Time series data were processed into the frequency domain using the procedure detailed in Myer et al. (2011) and summarized here. Data were fast Fourier transformed (FFT) into the frequency domain using a nonoverlapping time window that is exactly one waveform long and synchronized with the receiver's minute mark. Because the source waveform also is synchronized with the minute mark and both clocks are independently synchronized to GPS time — the transmitter is synchronized continuously during transmission and the receiver at the beginning and end of deployment — we expect that the receiver phase will be well controlled and near zero at close approach of the transmitter. (The phase is primarily a measure of signal delay and at close range the delay is nearly zero or 180°, depending on the specific field component.)

To suppress spectral leakage due to the red spectrum caused by time variations in earth's electromagnetic fields, data are prewhitened by first-differencing prior to the FFT, then postdarkened in the frequency domain to remove the effects of the first difference operation (Keisler and Rhyne, 1976; Shumway and Stoffer, 2000). Instrument specific calibrations are applied in the frequency domain and electric field data are normalized by the receiver dipole length. All data are presented in the phase "lead" convention (i.e., phase becomes more negative with increasing attenuation).

To calculate the CSEM transfer function, we divide the receiver data by the transmitted source dipole moment (SDM). Because SUESI is a constant voltage source, changes in the electrode impedance (i.e., through ablation) change the output current. Thus, the SDM varies somewhat throughout the tows. While some commercial sources collect recordings of the transmitter output current at a high enough frequency to deconvolve with the receiver data directly, the present version of SUESI only records the output current every three seconds. We use this to build a piecewise linear model of the current over time. The receiver field data are divided by this model and by the length of the transmitter dipole to yield final units of V/Am^2 for the electric field transfer functions and nT/Am for the magnetics. The standard deviation of the current measurements from the linear models is 2%, but this is artificially high. We record the rms of instantaneous current measurements taken over a three-second interval and this includes a varying number of polarity transitions. Though the transitions are brief, they represent outliers to which the rms calculation is especially sensitive. The actual

uncertainty in the SDM as estimated from high-frequency snapshots of the waveform is probably less than 0.5%.

The next step in processing is to correct for the frequency-dependent scaling of the source waveform. Waveform D has a closed-form mathematical solution for its complex scaling coefficients. However, the theoretical model requires that the switching in the binary waveform occur in zero time, a feat which is not obtainable with actual electronics. To quantify the effect of finite-time switching, we periodically recorded high-frequency snapshots of the waveform measured by an on-board current clamp at the output of the transmitter. Figure 5a shows one such snapshot recorded at 600 Hz. SUESI uses fast-switching insulated-gate bipolar transistors that enable it to switch polarity in the waveform without stopping at zero output current (as some previous EM transmitters, see for example Sinha et al., 1990; Constable and Cox, 1996). Figure 5b shows one transition sampled at 3600 Hz. The polarity change occurs in 1.7 ms and takes an additional 10 ms to settle to its full value. The transmitter creates the output waveform from a rectified 400 Hz power source. This introduces an 800 Hz ripple into the instantaneous output current, visible in the figure, which has been smoothed out by the inductance of the antenna. Further attenuation of the 800 Hz ripple occurs in the seawater associated with the ~10 m skin depth at this frequency.

Multiple snapshots were taken throughout towing and show that the theoretical and practical waveform differ by less than 1%. Furthermore, the waveform changed less than 0.3% over six and a half days of continuous transmission, even as the transmitter electrodes ablated. We used complex coefficients calculated from the median of the snapshots to scale the transfer functions.

The transfer function data were then phase corrected for linear drift calculated for each receiver's clock determined by time synchronization with a reference GPS clock. Figure 6 shows a histogram of time drift values for all receivers in the Scarborough survey. The distribution is steeper than Gaussian with 50% of the deployments having drift rates between ±1.5 ms/day and 79% having rates within the instrument clock specification of ±4.3 ms/day. The time drift introduces a frequency-dependent phase shift, which we correct in the frequency domain under the assumption that the drift is linear over the course of each deployment.

Data were binned to one data point per minute using an arithmetic mean. We chose a 60 s stack length to provide enough data samples (15) for statistical determination of noise while keeping the total change in along-track range relatively short (~45 m in this case). The signal-to-noise ratio (S/N) of far range data could be improved by using longer stacking bins. We have chosen not to do that in this work to keep the overall error analysis uniform. Variances for each stack bin were calculated using the Bienaymé formula on the differences between the amplitudes of the data and a linear trend through them. To first order, this allows the variance to account for actual scatter in the data without being biased by exponential decay. We find that for ranges greater than ~1.5 km, this variance accurately reflects the noise floor of the instrument at each frequency (Figure 7). At closer ranges, the variance shows the increasing bias from the finite length of the dipole and the changing range of the transmitter.

Pseudosections

Pseudosections of the normalized amplitude data provide a qualitative observation of the performance of each frequency in the detection of the Scarborough reservoir and are a useful approach

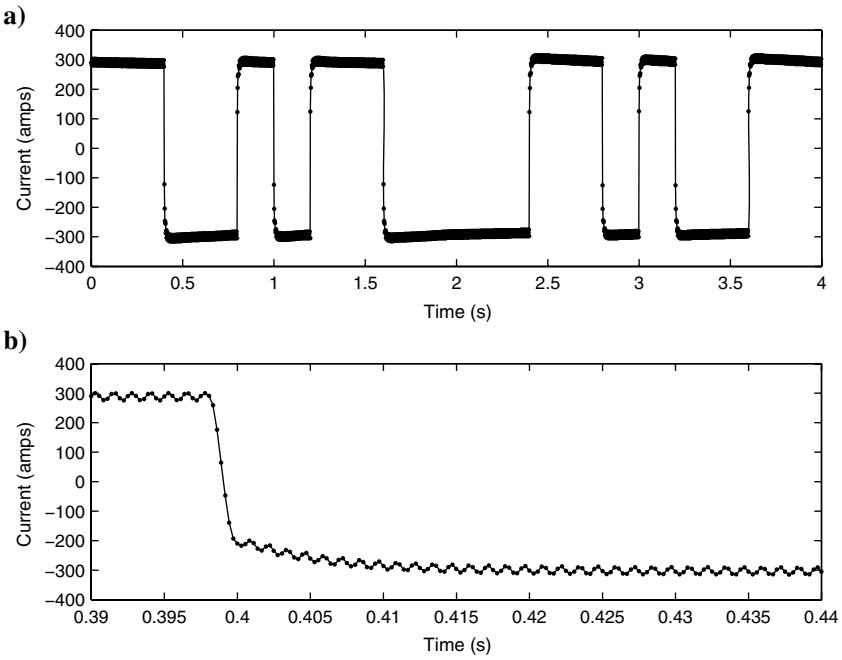

Figure 5. (a) Measurement taken at 600 Hz of the electric current forming the waveform that we used in this experiment. The waveform is scaled to four seconds so that the fundamental is 0.25 Hz. (b) One transition in the waveform sampled at 3600 Hz. The transition takes 1.7 ms with a further 10 ms to settle to its full value. The receivers are recording a data point every 16 ms, so the entire transition occurs in one sample datum. Also visible is the 800 Hz ripple caused by the rectified 400 Hz power source. Most of the ripple has already been smoothed out by the inductance of the antenna during transmission.

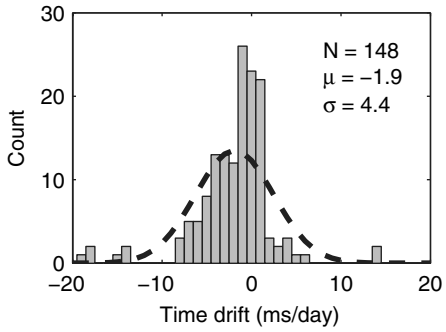

Figure 6. Histogram of the time drift calculated for all receiver deployments. The outliers (> ± 10 ms/day) are due to an operator error during the startup of the receiver instruments. The dashed line is an ideal Gaussian which has the same mean, standard deviation, and sample size.

for rapidly identifying lateral variations in the data. Inline electric field amplitudes for the pseudosections are normalized by the 1D model response of the off-reservoir Scarborough geology and placed in 200 × 200 m bins. Each bin is centered at the *x*-axis location corresponding to the midpoint between the transmitter and receiver and the *y*-axis location corresponding to the range (source-receiver offset). A gridding algorithm averages the bins and fills empty neighbors with linear interpolants. Data with a S/N less than two are not shown.

Figure 8 shows the pseudosections for line two and lines three and four, projected onto easting and northing lines, respectively. The color scale is the ratio of the observed amplitudes to the normalizing 1D background, such that a value of two indicates a 100% anomaly. Because CSEM is volume sampling, anomalies from resistors of large extent tend to get stronger with range as more of the anomalously resistive body enters the volume being sampled by each datum.

The pseudosections agree with our prediction that the 0.25 Hz frequency is relatively insensitive to the reservoir compared to the other frequencies. They also show an anomaly that is clearly

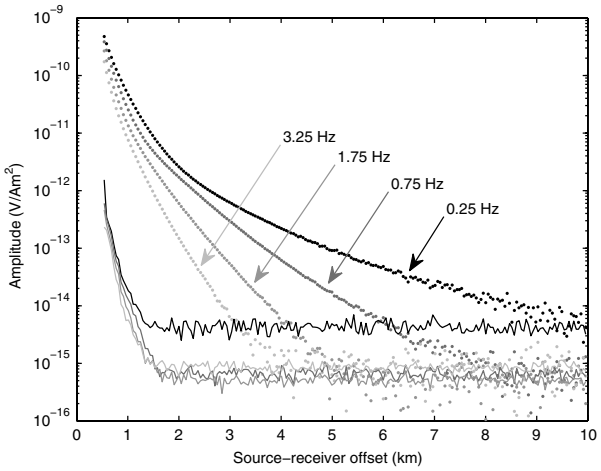

Figure 7. Site 1 amplitudes (points) and standard deviations (lines) for the 60 second stacks of the four strongest harmonics: 0.25, 0.75, 1.75, 3.25 Hz. The ramp in the standard deviation at close ranges is due to biases from the finite dipole and stacking.

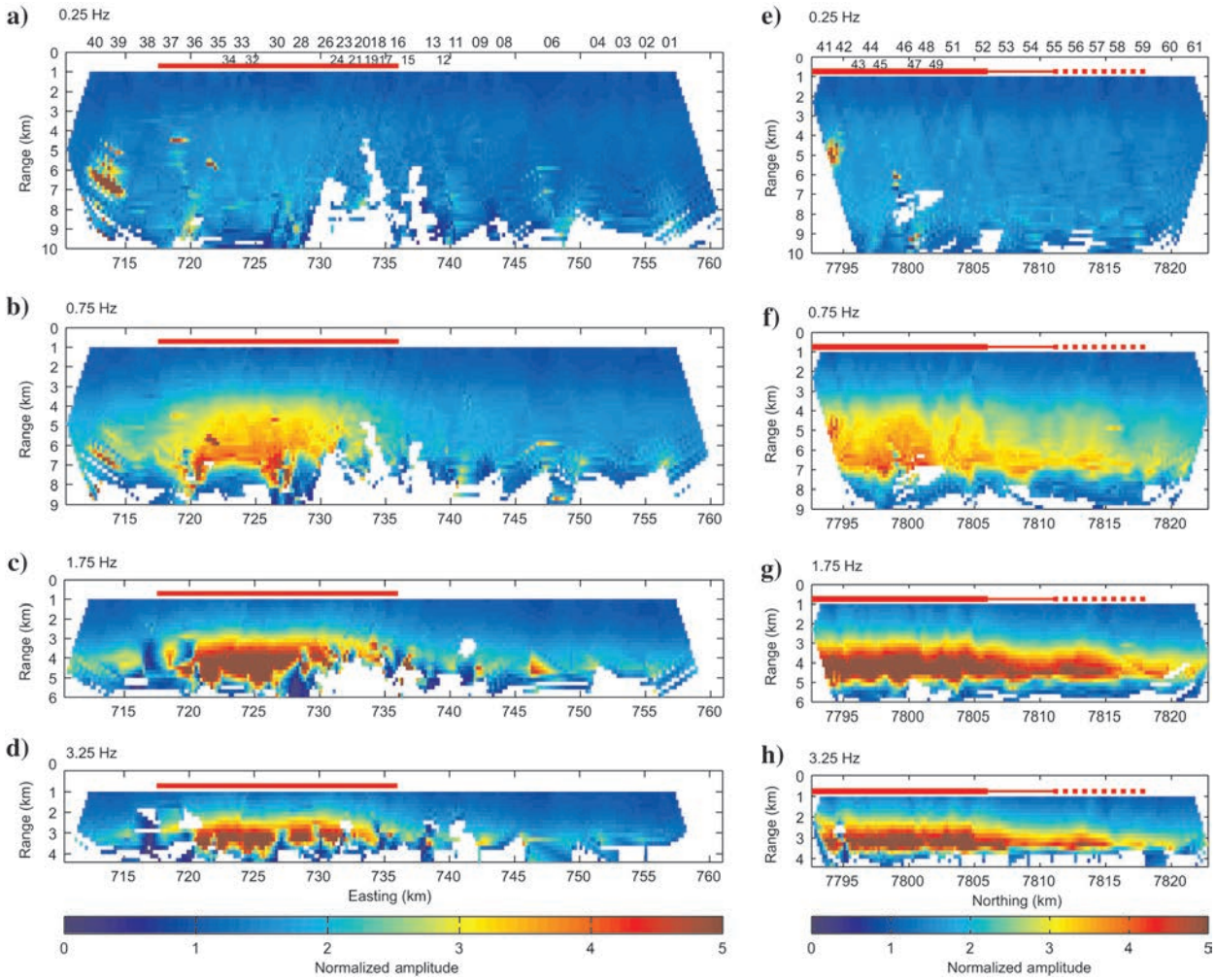

Figure 8. (a-d) Amplitude pseudosections for line two projected into UTM easting and (e-h) lines three and four projected into northing. All pseudosections are normalized by the 1D off reservoir background in Figure 2. In line two, the thick red line marks the expected extent of the reservoir; in lines three and four, the line thins where the reservoir narrows, and is dotted where the reservoir splits into the rabbit ears. All figures have 1.5 × vertical exaggeration. Data below a S/N of two have been cut out. As predicted by forward modeling, the sensitivity to the reservoir increases with increasing frequency.

stronger with increasing frequency as predicted, even though the usable range is declining. Assuming the 1D normalizing model is correct, the line two pseudosections (a-d) place the reservoir anomaly between 718 and 734 km easting, which agrees quite well with the geologic prediction. The higher frequencies, however, continue a 60%–80% anomaly across the line. This anomaly may indicate that the geologic background model underestimates the resistivity of some layers, particularly the resistive Gearle siltstone. On the other hand, the reservoir outline in Figure 1 is not the precise edge of the reservoir, merely the boundary inside which gas saturation is expected to be above 50%. It may be that the CSEM data are sensitive to the lower gas saturated volume outside the outline.

The lines three and four pseudosections (e-h) strike northeast across the body of the reservoir and along the easternmost of the "rabbit ears." The anomaly decreases starting at 7806 km northing, corresponding to a narrowing of the reservoir body about 5 km before the "ears" begin. It is likely that the saturation or thickness of the reservoir begins to decline here, though according to the two highest frequencies, this is a step, not a gradual change toward the edge, indicating the possible location of a structural control on the migration and trapping potential of the reservoir or variations in the deeper source region.

ERROR ANALYSIS

Location uncertainties

The most significant sources of uncertainty in CSEM data are typically the errors in the position and orientation of the receivers and transmitter. Positions are determined by acoustic ranging using a sound velocity profile of the water column. Changes in the water column may alter the sound velocity, so it is important to use local measurements to reduce location errors. The Valeport Midas SVX2 instrument mounted on the body of our transmitter continuously measures sound velocity, pressure, temperature, and conductivity. Though the bulk of this time is spent near the seafloor, the transmitter was raised into the water column for every turn and traversed the entire column at the beginning and end of each phase. We found that the sound velocity profile was similar throughout the survey, varying by about 1 m/s at a given depth. A composite sound velocity profile was created from these measurements by binning the data in 10 m bins from 0 to 500 m depth, where the thermocline gives rise to a sharp gradient, then 100 m bins below that. The resulting profile is constructed from the median of each bin and the upper 500 m is smoothed. The final sound velocity profile is shown in Figure 9, along with a conductivity profile that is constructed using the same procedure. Smoothing is required on the conductivity profile to match the shape of the 24 expendable bathy-thermograph (XBT) casts taken during the survey, and so we apply it to the sound velocity profile as well.

Receiver locations were determined by long base-line acoustic ranging from the ship. For each instrument, there are 40–200 range data points acquired from a variety of ship positions. These data points, along with GPS ship positions (referenced to WGS-84), were then used in a Levenberg-Marquardt raypath inversion to solve for the best-fitting receiver location. The covariance matrix from this inversion yields 2σ uncertainties on 95% of the site locations of 7 m horizontally and 2 m vertically (Figure 10a). The northing and easting components have similar distributions. The vertical component is more tightly constrained because of the steepness of the acoustic raypaths.

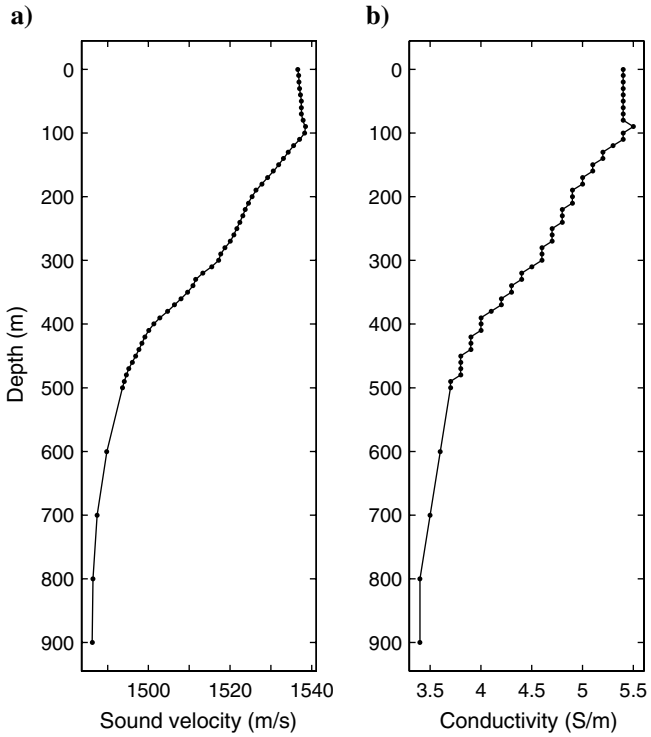

Figure 9. Composite (a) sound and (b) conductivity profiles for the ocean overlying the Scarborough gas field, created as described in the text.

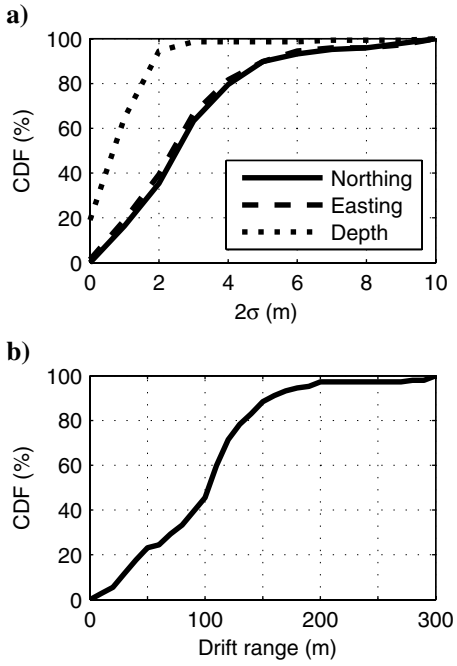

Figure 10. (a) The cumulative distribution functions for the 2σ errors on receiver positions determined by a Levenburg-Marquardt raypath inversion. (b) Cumulative distribution function of the drift in range between drop location and landing location for each receiver.

In general, during the 950 m free fall through the water column, half of the receivers drifted horizontally more than 100 m from their drop locations (Figure 10b), which indicates the presence of strong currents. Industry practice is to reject any deployment that is farther than 50 m from the planned location. To accomplish this, the ship must stand by and wait for a receiver to reach the seafloor, navigate it, then offset the ship position for the next deployment to account for the observed drift. Because drift varies over time, the drift "forecast" must be updated sequentially and receivers that land outside the tolerance zone must be recovered and redeployed. For a large survey such as Scarborough, this adds several days of ship time at considerable cost. For this project, such deployment accuracy is not required; inline field components will not be biased by instrument drift because the navigated locations are so well known, and modeling shows that 100 m of crossline set has a small effect on inline field components (<0.5%).

Receiver orientations were measured directly with a compass mounted in a separate pressure case high on the instrument frame where it is less likely to be influenced by the receiver electronics. The magnetic compass measures the instrument frame orientation and does not account for any unintended bending of the electrode arms. We performed an independent verification of the compass orientations using the orthogonal Procrustes rotation analysis (OPRA) method described in Key and Lockwood (2010). This method works by simultaneously inverting for the seafloor conductivity and the optimal rotation matrix between the observed data and the data predicted by the conductivity model. This approach allows the OPRA method to find the orientation of inline and offline receivers and does not require any a priori assumptions about component polarizations. Here, we applied the method to the 0.25 and 0.75 Hz data at ranges of 14 km, including in- and out-tow data. In general, the inversion was able to find the orientations within only a few iterations and most data could be fit to rms 1.0 using an error floor of 10%. Comparing the OPRA-derived orientations with those measured by the compasses (Figure 11), we estimate the 2σ orientation error to be 6.6°. For inline field components, this equates to less than 0.7% uncertainty.

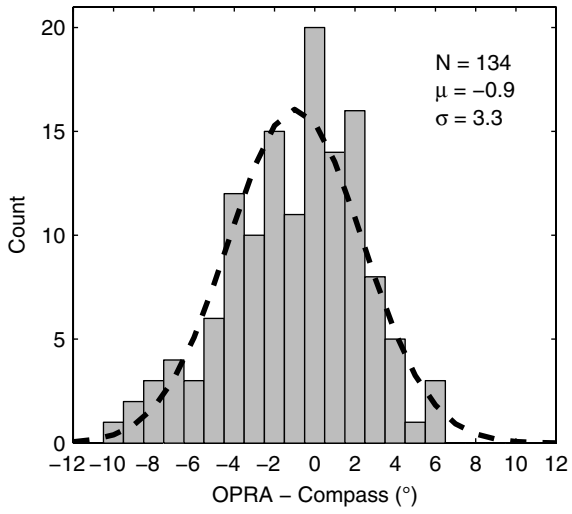

Figure 11. A histogram of the differences between the receiver orientations measured with an in situ magnetic compass and those derived from the OPRA method. The dashed line is an ideal Gaussian which has the same mean, standard deviation, and sample size.

Transmitter locations were determined with the iLBL system. Individual point solutions were then smoothed into a transmitter track and the uncertainties of the inline and crossline locations were taken to be the standard deviation of the point solutions from the smoothed track.

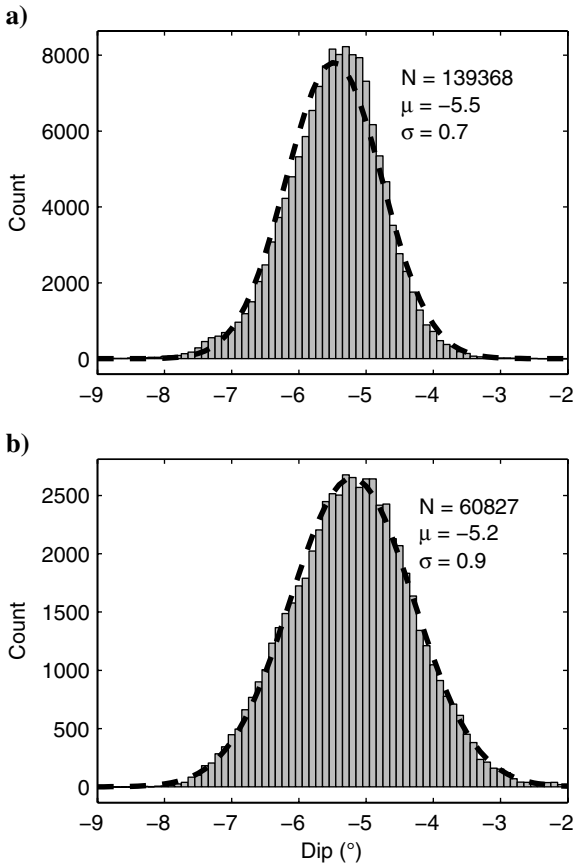

Figure 12. Histograms of dip calculations for (a) phase two and (b) phase three overlain with an ideal Gaussian (dashed line) which has the same mean, standard deviation, and sample size. Dip calculations are based on the difference between pressure gauges mounted at the transmitter body and the beginning of the far electrode. For both phases, the standard deviation in dip is less than 1° and the average is more than −5°, where negative indicates the head is above the tail.

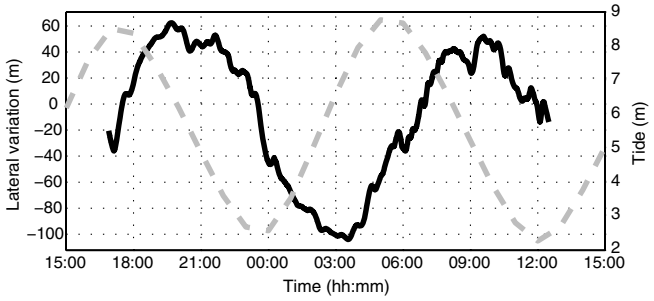

Figure 13. Lateral variation of the transmitter with respect to the ship's track line for line two (black) superimposed with tides (gray, dashed) for Broome, WA ~1000 km east of Scarborough. The *x*-axis is shown in time so that tidal nature of the lateral variation is more evident. (Tide data from the Australian Baseline Sea Level Monitoring Project at http://www.bom.gov.au/oceanography/projects/abslmp/data/index.shtml).

The iLBL system uses acoustic ranging to solve for the location of the acoustic unit on the tow vehicle, but not the center of the dipole antenna trailing behind it. The center of the dipole is the more pertinent value for modeling and inversion, so we estimate its location using the following procedure. For this survey, the near electrode of the dipole began 11 m behind the acoustic unit and consisted of 100 ft of soft copper pipe rigged with syntactic foam to be approximately neutrally buoyant. The far electrode began 261 m behind the acoustic unit and was identical to the near electrode. We calculated the location of the center of the antenna to be 151 m behind the tow vehicle along a straight horizontal line extending from the ship through the transmitter. For phase four, which targets an area of suspected hydrates, the distance to the far electrode was shortened to 61 m and the copper electrodes were cut down to 10 m, so that the center of the dipole was 41 m behind the transmitter.

The dipole is given a dip corresponding to the difference in depth measurements derived from pressure gauges mounted on the transmitter and at the beginning of the far electrode. We convert pressure to depth using the procedure outlined in Leroy and Parthiot (1998). We measured dip in phases two and three (Figure 12) and found it to be remarkably stable: $-5.5 +/- 0.7$ and $-5.2 +/- 0.9°$, respectively, where negative dip indicates that the far electrode is deeper than the near. We attribute the stability to the flat bathymetry. Though we were towing to achieve a constant altitude, we were able to keep changes of the transmitter depth to a minimum, thus allowing the dipole assembly to trail unperturbed through the water. For phases two and three, we use the dip time series. However, for phases one and four where we do not have dip measurements, we use a fixed-dip value of $-5.4°$. Additionally, we observe in phases two and three that it takes about eight to 10 minutes for the antenna to settle after the transmitter has reached the target depth, so there may be up to 15° of error in dip in the first 10 minutes of tow for phases one and four, which is not accounted for by the fixed value.

In the absence of acoustic positioning, we assume that the azimuth of the transmitter dipole lies along a line between the transmitter and the ship. On average, 1600 m of 0.680" deep-tow cable

Table 1. Transmitter uncertainties for each tow line. Standard deviation in dip and azimuth measurements are projected into depth and crossline set, respectively. The variation calculations for dip exclude the first 10 minutes of tow when the antenna is settling. Dip was not measured in phases one or four, but the variation is expected to be less than 1° like the other tow lines. We expect the depth uncertainty in phase four due to dip to be negligible because it uses a much shorter dipole. Total crossline uncertainty is calculated from the quadrature of the iLBL and azimuth uncertainties. Error in depth from the pressure gauge is negligible for all phases as is the inline error from dip and azimuth variations.

	Dip		iLBL		Azimuth		Total
Line	σ (°)	Depth (m)	Inline (m)	Cross (m)	σ (°)	Cross (m)	Cross (m)
Phase one							
1	—	—	—	—	—	—	—
2	—	—	2.7	8.2	2.6	6.8	10.7
3	—	—	3.2	6.8	1.2	3.2	7.5
Phase two							
4	0.6	1.6	2.8	5.7	2.6	6.9	8.9
4a	0.7	1.8	2.0	3.8	3.5	9.1	9.9
5	0.5	1.3	2.7	5.6	3.2	8.5	10.2
5a	0.5	1.3	2.1	4.5	1.8	4.8	6.6
6	0.7	1.8	3.2	7.1	2.1	5.6	9.0
6a	0.7	1.8	1.6	3.7	1.6	4.3	5.7
7	0.6	1.6	3.4	5.9	2.2	5.8	8.3
7a	0.5	1.3	3.6	4.0	3.7	9.8	10.6
8	0.8	2.1	2.8	7.1	2.8	7.2	10.1
9	0.4	1.1	2.8	5.4	1.7	4.4	7.0
10	0.5	1.3	2.4	5.5	2.5	6.5	8.5
11	0.6	1.6	2.6	5.9	2.5	6.7	8.9
Phase three							
12	0.9	2.4	2.2	6.5	1.7	4.4	7.8
12a	0.6	1.6	3.2	6.0	2.4	6.4	8.8
12b	0.8	2.1	2.2	6.5	1.4	3.8	7.5
13	0.9	2.4	4.1	6.6	1.2	3.3	7.4
Phase four							
14	—	—	2.8	4.3	0.9	0.6	4.3

was deployed and this corresponds to a sail of ~28 m^2 being pulled sideways through the water. Friction with the water should keep the azimuth of the transmitter equal to the direction of motion; however, the iLBL navigation revealed significant lateral variation in the location of the transmitter with respect to the track line of the ship, so there is some ambiguity in the azimuth of the antenna dipole. Figure 13 shows that the crossline variation of the transmitter position with respect to tow line two is up to 100 m. The other lines have similar variations. The tides measured at Broome, West Australia, 1000 km east of the survey area are overlaid in the figure and show that these variations almost certainly are related to tidal action. Because the insulated cables carrying electric current to the electrodes have a large cross section, presenting an additional ~15 m^2 to orthogonal currents, it seems likely that deep currents are responsible for the lateral variation. Accordingly, we assume the uncertainty in the transmitter azimuth to be approximately equal to the difference between the transmitter azimuth and line azimuth. The standard deviation of the difference between all line and antenna azimuths is 3.2°. Using the law of cosines, this is an 8.4 m crossline variation and a negligible inline variation. Though the azimuth ambiguity relatively is inconsequential for the inline data, it can be a large source of uncertainty for the crossline data and thus for full 3D interpretation of this data set.

Table 1 summarizes the transmitter uncertainties for each tow line. We have projected the uncertainty in azimuth into the crossline direction and the uncertainty in dip into depth. Uncertainty in depth from the pressure gauges is at the centimeter scale and therefore, ignored. For total crossline uncertainty, we add the uncertainties from the iLBL solutions and the azimuth (projected into crossline) in quadrature.

Environmental noise

In phases one through three, we deployed LEMs with 100 m dipoles, which are ten times longer than the dipoles on the OBEMs. If the dominant source of noise is from the electrodes and amplifiers, or other instrumental voltage sources, then one would expect an improvement in S/N that is proportional to antenna length. Because the LEMs and OBEMs use the same electronics, the longer dipole on the LEM should provide a factor of 10 improvement in the noise floor at all frequencies. However, we find that the noise floor of the LEMs is lower than the OBEMs by a factor, which is less than the expected value of 10 and increases with frequency. Table 2 shows the noise floor for LEM 2 (which has a slightly lower noise floor than LEM 1) and a low-noise OBEM chosen from each phase, as well as the ratio of the two. While the OBEM noise floors varied between 30% and 70% across the three phases of deployments, the LEM noise floors varied much more widely and were significantly lower in phase one. This suggests that the LEM data are limited by environmental noise rather than electronic noise. The low variability in OBEM noise floors at the higher CSEM frequencies (> 0.75 Hz) may indicate that the noise source is at or below the noise floor of these frequencies and that their data mostly are limited by electronics.

At frequencies below the CSEM range, spectrograms of the OBEM data show a periodic increase in noise at intervals that match the tidal cycle (Figure 14a) and die off as the tide amplitudes decrease, lending support to the idea that environmental noise is present. This pattern is common to many of the receivers and leads us to recommend that marine CSEM and MT surveys be planned for times of lower tidal amplitude. On the spectrogram for LEM1 (Figure 14b), these noise intervals only faintly are observed, indicating that, for the OBEMs, some of the noise is motional. Additionally, we observe occasional noise bursts on some OBEMs that raise the noise floor by a factor of 10 or more for a few hours. Curiously, two such events are captured simultaneously at sites 14 and 15, which are spaced 1 km apart in line two. While noise on a single site might be attributed to the electronics, contemporaneous noise must be environmental.

Table 2. Noise floors and noise floor ratios for LEM 2 and OBEMs from phases one through three. LEM 2, which has a consistently lower noise floor than LEM 1, is compared with representative sites from phases one through three (sites 1, 96, and 110, respectively). The ratio should be 10 because the LEM dipoles are ten times longer. Variation with frequency and deployment indicates that the instrument noise floors are limited by environmental noise, not equipment. The noise floor is from the mean of the stacking variance on in-tow data at ranges greater than 2 km.

Frequency	Instrument	Line two	Line eight	Line 12	Maximum variation
0.25 Hz	OBEM	4.2e−15	5.4e−15	3.1e−15	74%
	LEM 2	1.9e−15	3.1e−15	2.4e−15	63%
	ratio	2.2	1.7	1.3	
0.75 Hz	OBEM	6.6e−16	7.1e−16	4.7e−16	51%
	LEM 2	2.0e−16	3.6e−16	4.1e−16	105%
	ratio	3.3	2.0	1.1	
1.75 Hz	OBEM	5.1e−16	5.6e−16	4.1e−16	37%
	LEM 2	0.74e−16	1.8e−16	2.1e−16	184%
	ratio	6.9	3.1	2.0	
3.25 Hz	OBEM	8.4e−16	9.5e−16	7.0e−16	34%
	LEM 2	1.0e−16	1.9e−16	2.3e−16	130%
	ratio	8.4	5.0	3.0	

We suggest that the source of environmental noise is related to the movement of localized currents in the ocean, e.g., internal waves induced by tidal flow over bathymetry (Lim et al., 2008; Van Gastel et al., 2009). Usually, in CSEM, this takes the form of shaking of the instruments by the water moving over them. Though the noise on the OBEMs might be attributable to this, the LEM noise is unlikely to be motional. Unlike the OBEM electrodes which are housed in weighted, semi-rigid poles and may move when the instrument body is moved, the LEM electrodes are attached to loose, negatively buoyant cables. Motion on the LEM body does not translate down the cable, so shaking the electrodes requires that they be lifted out of the mud at the seafloor. If the LEM noise, the low-frequency tidal noise, and the burst noise all come from the same source, which seems logical, it is unlikely to be limited to motion of the instruments. Possible additional sources are induction from the ocean moving across the instruments and microseisms (Webb and Cox, 1984, 1986; Webb and Constable, 1986).

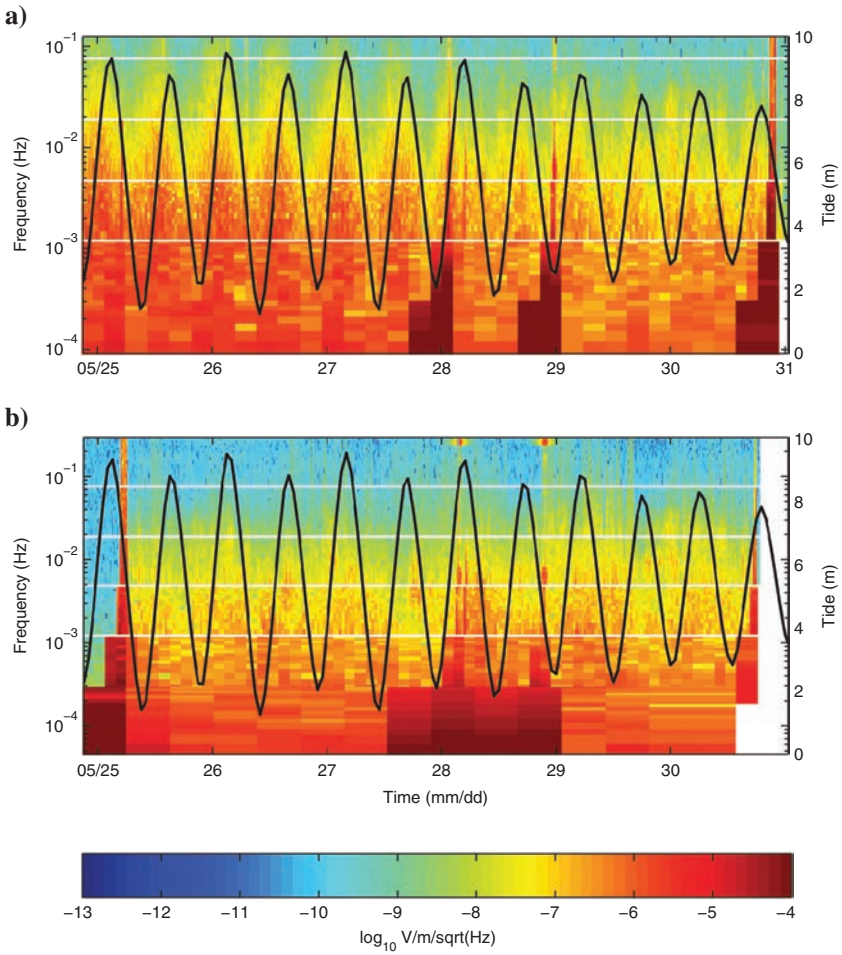

Figure 14. Spectrograms from phase one of (a) the ex-channel from site 11, and (b) one of the channels from LEM1 at site 7, overlain with the tides observed at Broome, 1000 km to the east in West Australia. The regularly occurring increase in the power in the spectrum is an increase in noise which is correlated with the tides. The electric field noise decays in strength as the magnitude of the tides lessens. This noise source is less clear in the LEM indicating that the OBEM noise involves instrument motion. The saturated segments of the spectrogram near midnight on the 28th and 29th of May are passes by the transmitter. Saturated segments at the beginning and end are from the receiver traversing the water column.

Data repeatability

We performed two tests in the Scarborough survey on the repeatability of data acquisition that provide important information on the level of random noise in the data and the aggregate effect of the position uncertainties. In the simpler of the two tests, we towed a line of sites in opposing directions — lines 12 and 13. Because the receivers remained in the same locations for this test, any difference in the out-tow of one line with respect to the in-tow of the other line will be due almost entirely to random noise and the uncertainty in the transmitter position, azimuth, and dip. This allows us to quantify the average effect of these uncertainties. There may be an additional effect due to the heterogeneity of the near-surface strata because the corresponding in-tow and out-tow positions are not over exactly the same portion of seafloor. However, the difference in positions is only on the order of a few tens of meters which will produce an insignificant effect when the range is over about one kilometer. We constrain the test data to ranges greater than 2 km to avoid bias from the finite dipole and the motion of the transmitter. We also impose a maximum range of 6 km and a minimum S/N of 10. We carried out the comparison outlined below with several frequencies and found that 0.25 and 0.75 Hz yield similar results, while higher frequencies do not have high enough S/Ns at intermediate ranges to produce relevant statistics. Here, we discuss the results for 0.25 Hz.

Data from two tows cannot be compared directly because of small changes in transmitter altitude, dip, azimuth, and crossline position. For example, if the antenna dip is 5° for lines 12 and 13, then because these lines are in opposite directions, there is a 10° difference in dip between a datum from line 12 and its corresponding datum in line 13. A comparison of the data would result in large variations, which are due to the value of the transmitter parameters, not their uncertainties. To remove these effects, we calculate the percent difference between each line's data and a reference 1D model in which the estimated transmitter position and orientation are used. By differencing the variation of the two tow lines from the model, we derive a comparison of the two data sets, which is a function of the uncertainties of the transmitter parameters while being independent of the specific values of the parameters. If, for example, the two lines have identical data, then their variation from the model will be identical and the difference between them will be zero. If one line is 1% lower than the model and the other line is 1% higher than the model, then the difference in the two data sets is 2%, independent of the transmitter orientations in the model.

Because the CSEM data are complex, there are two components for each datum; real and imaginary, or amplitude and phase. It is typical to assume an equal error distribution between the components. For noise, this is mathematically correct because the Fourier transform is a linear

operation. However, errors from position and orientation do not map equally in amplitude and phase. Error in transmitter dip, for example, has twice the effect on amplitude as on phase at intermediate ranges. For completeness, we use our procedure to evaluate amplitude and phase, and for the sake of comparison, we convert degrees difference to percent difference.

We note that many workers prefer to use real and imaginary to avoid the problem of "phase wrapping"; i.e., the data value is 356°, but the model value is 1°, which appears to be a difference of 355°, but is, in fact, merely 5°. Because transmitter uncertainties do not map equally in amplitude and phase, using them in real and imaginary requires the use of a full covariance matrix. We remind the reader that real and imaginary are a Cartesian projection of the more natural components of amplitude and phase, which are in polar coordinates. It is simpler to use amplitude and phase with distinct uncertainties and apply the few lines of code required to account for phase wrapping than to implement a full covariance matrix for real and imaginary components. This is the approach we take in this and the companion work.

Figures 15a and 15b shows histograms of the amplitude and phase differences for 2 to 4 km range. Each histogram is overlain by an ideal Gaussian curve with the same mean, standard deviation, and sample size. At these short ranges, the S/N is well over 100, so the effects of random noise are small. The standard deviation, and therefore, the joint error from the transmitter uncertainties and random noise, is 2.8% in amplitude and 2.4% (1.4°) in phase. Additionally, there is a bias of 0.3% and 1.3% (0.7°), respectively, which may indicate a systematic error in one or more transmitter parameters. This bias is not surprising because a smoothing function is used on the iLBL point-to-point solutions and one of the drawbacks of a smoothing function is that while suppressing randomness it may introduce a systematic bias. The small size of the bias we measure indicates that the smoothing step may not be a significant source of error.

The effects of random noise may be seen in the longer ranges. Figures 15c and 15d shows the same comparison, but not for 4–6 km ranges where the S/N declines from about 80 to 10. The bias has not grown significantly in either amplitude or phase, but due to the increase in random noise, the standard deviation is approximately double.

The differences in the amplitude and phase uncertainties may provide some clue as to systematic errors in transmitter parameters. We investigate this by perturbing the transmitter parameters then comparing lines 12 and 13 again, constraining the range to 2–4 km to minimize the influence of random noise.

Replacing the calculated transmitter azimuth with the tow line azimuth increases the amplitude bias by 0.3% without affecting the other errors, indicating that the data prefer the azimuth to be along a line between the ship and transmitter, not along the ship track.

Perturbing the transmitter altitude of both lines has no effect on the comparison because the electric field variations are symmetrical. However, an asymmetric perturbation in which the altitude for line 13 is lowered by 1 m but line 12 is not changed, reduces the amplitude bias to 0.1% and the phase bias to 1.0%. This may explain a small portion of the difference in bias behavior between amplitude and phase, but cannot explain all of it.

Crossline perturbations have only a slight effect for large variations (0.3% over 100 m) and cannot be reasonably constrained by this test. However, perturbations of dip and inline distance have a large effect on the error structure, producing a bimodal distribution due to large asymmetry in the in-tow and out-tow portions of each site's data. Because our original comparisons are not bimodal, we can use the appearance of two lobes in the perturbed distributions to place outer limits on the systematic errors in the dip and inline distance.

Using this procedure, we find that the dip is the most tightly constrained parameter. A perturbation of $+1°$ (i.e., raising the far electrode with respect to the near electrode) raises the amplitude difference from 2.8% to 4.6%, while a perturbation of $-3°$ raises it to 6.3%, both due to the introduction of two lobes into the distributions. Interestingly, a perturbation of $-1°$ lowers the amplitude difference slightly to 2.5% while also lowering the bias from 0.3% to 0.1%. This may seem to indicate that this is a preferred configuration. However, the effect on phase is different; increasing the phase difference to 3.0% and creating a bimodal distribution. A

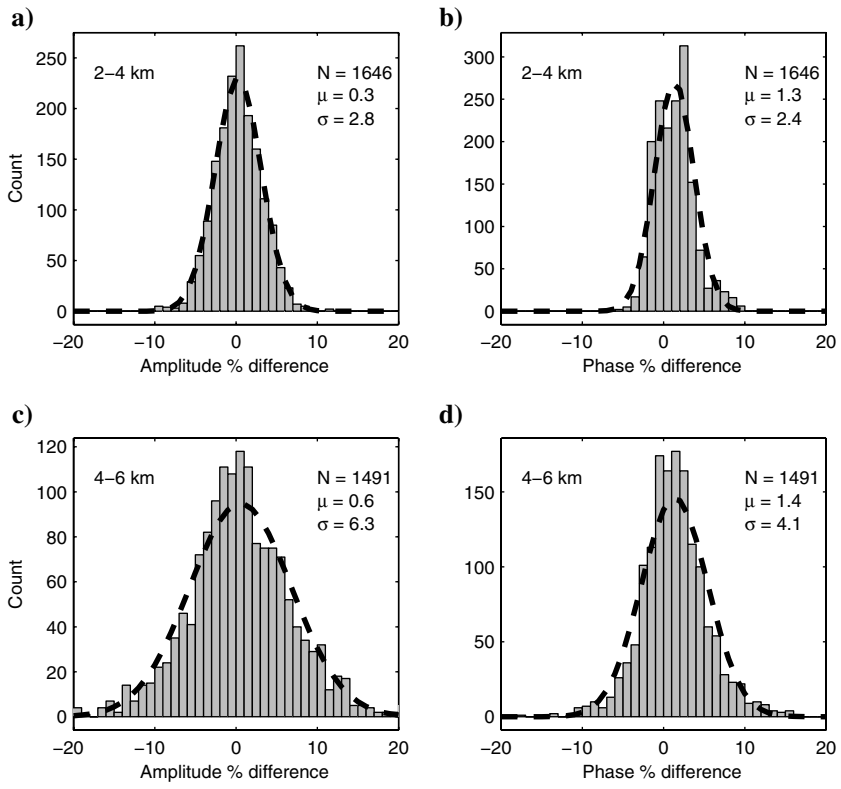

Figure 15. Histograms of the amplitude and phase differences between lines 12 and 13 for (a-b) 2–4 km, (c-d) 4–6 km. Each is overlain by an ideal Gaussian (dashed line) with the same mean, standard deviation, and sample size. The effect of the estimated transmitter orientation has been removed, leaving just the errors in transmitter parameters and random noise. For data in ranges 2–4 km, the S/N is >80, so the scatter is primarily from the transmitter navigation errors. The increase in scatter with increasing range is due to the growing influence in random noise.

+1° perturbation decreases the phase difference to 2.0%, but at +1°, the amplitude distribution is distinctly bimodal. Thus, the systematic error in dip is constrained to +/− 1° (Figure 16). This is likely a pessimistic estimate in view of the 0.9° standard deviation found for the entire set of phase 3 data (Figure 9b). When the perturbation is +/− 0.5°, the distributions are still somewhat bimodal, though not as clearly as at +/− 1°.

Inline range may be similarly constrained. The bimodal distribution develops more slowly than for dip but is observed in phase at a −5 m perturbation and in amplitude at +5 m (Figure 17), where negative indicates moving the transmitter closer to the ship. The amplitude difference between lines 12 and 13 is lowest when the perturbation is 5 m, but the phase difference is lowest when the perturbation is +10 m. Yet, these two minimums trade-off error in the other component, so we constrain the systematic error in inline range to +/− 5 m.

We carried out a second, more complicated test of data repeatability by redeploying and retowing instruments at two sites. Site 52 from phase one line three was redeployed with the same instrument in phase two line four and towed in the same direction. In addition to the random noise and transmitter position errors discussed above, differences in this redeployment also should contain the effects of errors in receiver location and orientation. Site 39 from phase one line two is more complicated because it was redeployed with a different instrument in phase three and towed in an orthogonal line. Differences at this redeployment will include the effects of variation in instrument calibration, as well as heterogeneities in geologic structure along the orthogonal lines. Site 39 is 4 km off the projected edge of the reservoir, so we expect geologic heterogeneities to affect the 4–6 km range data, but not closer ranges.

We applied the model-difference analysis to sites 52 and 39. For site 52, we have used only the in-tow data because during the out-tow there were changes in the line three transmitter altitude significant enough to cause changes in the antenna dip, and the dip in tow line three is unknown. For site 39, we compare the deployment of two different instruments in line two and line 12, which were towed in orthogonal directions. The difference for each redeployment is summarized in Table 3, along with the results from lines 12 and 13 for comparison.

The decline in bias with range observed at both sites may indicate that the bias is due to position error because rotation errors introduce a bias that is generally range independent. Presumably, this effect is not observed in the lines 12–13 comparison because the errors are random site-by-site and cancel in the comparison of those 23 sites. The single site redeployment differences are similar to those observed in the line comparison. Apparently, errors in instrument navigation and orientation introduce very little additional scatter in the data and only a few percent bias, which declines with range. Site 39, which might be reasonably expected to have larger differences due to one of its orthogonal tow lines being partially over the reservoir, is remarkably similar to the other comparisons. The higher values for its phase difference are probably due to the reservoir.

Over all, the differences in repeat tows and deployments give us a minimum error level of 3% to 6%, depending on range. Uncertainty from systematic navigational errors can be limited to +/− 1° in dip and +/− 5 m in range for systems which use iLBL navigation. We expect values similar to these to apply to any well-run survey and to be of guidance for users designing and participating in time-lapse surveys to monitor the evolution of a hydrocarbon field during exploitation (e.g., Orange et al., 2009). It is unlikely that changes in a target that produce less than a 3% to 6% change in the anomaly will be detectable unless additional measures are taken to constrain location errors.

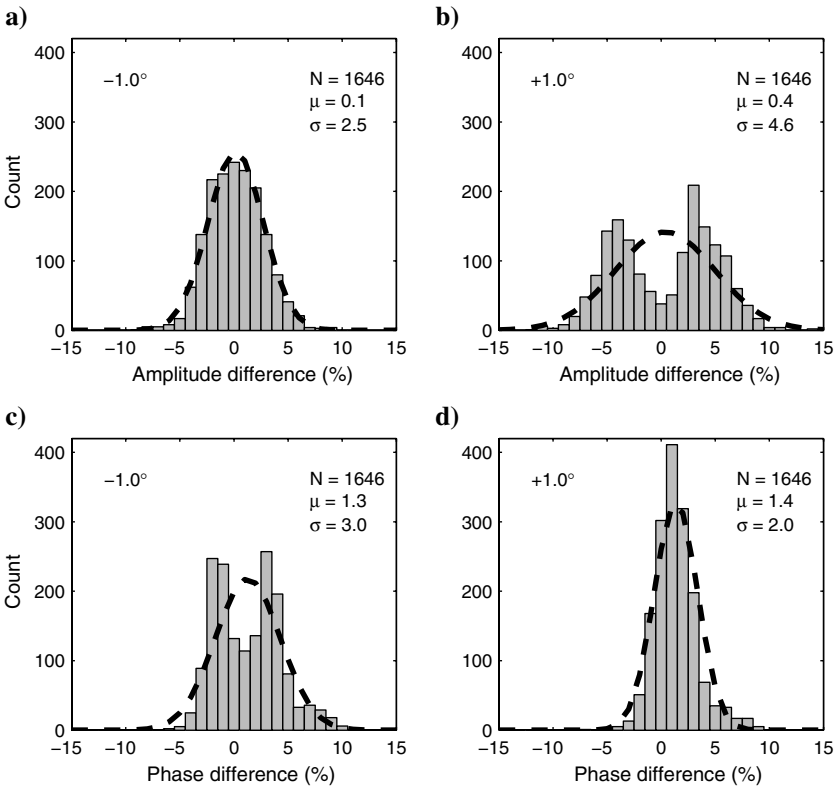

Figure 16. Histograms of the lines 12–13 comparison in amplitude and phase when dip is perturbed by −1° (a and c) and +1° (b and d). Each is overlain by an ideal Gaussian (dashed line) with the same mean, standard deviation, and sample size. The development of two lobes in the distribution identifies the maximum systematic error in dip as +/− 1°.

COMPOSITE UNCERTAINTY MODEL

We can reconcile the observed amplitude and phase variations with the estimated uncertainties in the transmitter parameters by forward modeling. We compare electric field amplitudes and phases computed from a 1D model of the reservoir, with fields generated on the same model but with one transmitter parameter perturbed by the uncertainties we have estimated from the Scarborough data. The base model uses the water conductivity profile from Figure 9 with the seafloor at 950 m, the transmitter 50 m above the seafloor, and −5.6° of dip. We modified the 1D code of Key (2009) to support a finite dipole source and calculate all models with a 250 m dipole. The finite length dipole was computed by Gauss quadrature integration of point dipole

fields along the true dipole length, where a quadrature order of 10 was found to be sufficient for the ranges considered here. For location perturbations, we use the uncertainties outlined in Table 4, which we have derived from the values in Table 1 and the discussion in the previous sections. We also have calculated the difference between the finite and point dipoles and included it in our analysis because many modeling codes use a point dipole and there is a range-dependent bias introduced by the dipole length. Note that in the Scarborough data, we use a 60-s stacking window that covers ~45 m of transmitter motion. Because this is much smaller than the dipole length, we ignore it in our calculations below, which are representative for phases one through three. However, in phase four, the dipole and stacking biases are comparable, so the stacking bias should not be ignored.

In Figure 18, we show the inline error that would be introduced in the 0.25 Hz amplitude and phase by each type of uncertainty, along with a composite curve in which all the components have been added arithmetically. We do not add them in quadrature because they are not independent. The effect of crossline distance is nearly zero at all ranges, so it has been left off the plot for clarity, but is included in the composite curve. Also, note that we show positive bias produced by the finite dipole, but do not add it into the composite curve. Because of the transmitter dip included in all models, there is a slight asymmetry between the in-tow and out-tow portions of the dipole bias and transmitter dip components. We show only the out-tow where the uncertainties are slightly larger.

Close range uncertainties are dominated by the dipole bias. After about 2 km range, the amplitude uncertainty is due mostly to dipping of the source dipole, which mixes the stronger horizontal fields with the weaker vertical fields, suppressing the amplitudes observed at the receivers. Phase uncertainty, however, is due mostly to altitude. In electromagnetic diffusion, phase is a proxy for propagation velocity, so small changes in the volume of water between the dipole and seabed translate into increased or decreased phase delay for all ranges because of the propagation velocity contrast between the ocean and seafloor. The minimum in the dipole bias and inline distance curves observed near 2 km is due to the −5.6° dip of the dipole. If the dipole were level, these minima would not appear.

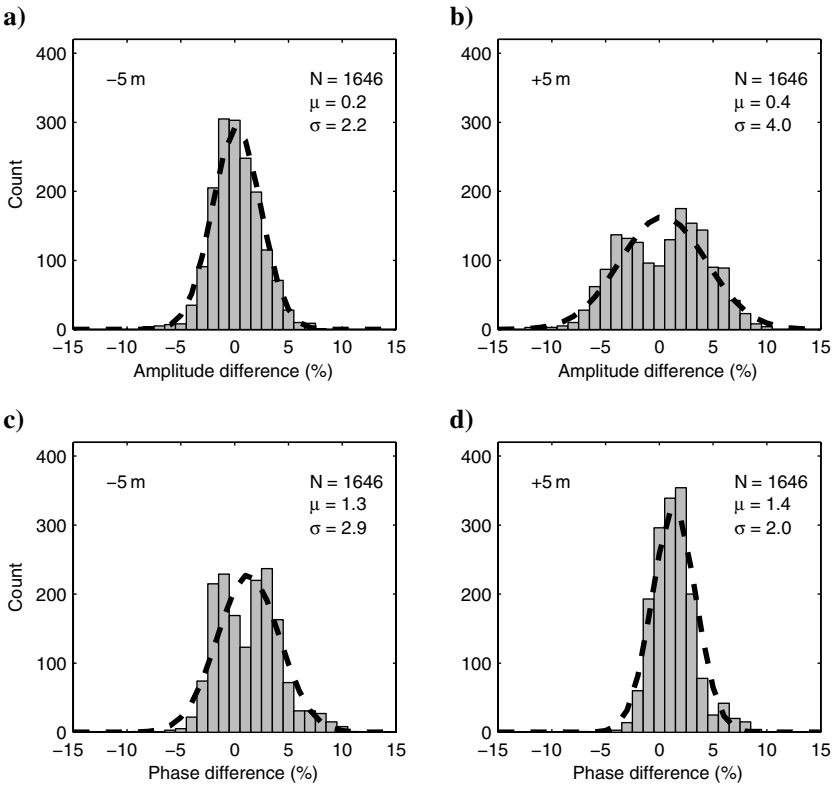

Figure 17. Histograms of the lines 12–13 comparison in amplitude and phase when inline range is perturbed by −5 meters (a and c) and +5 meters (b and d). Each is overlain by an ideal Gaussian (dashed line) with the same mean, standard deviation, and sample size. The development of two lobes in the distribution identifies the maximum systematic error in inline range as $+/-5$ m.

Table 3. Summary of redeployment uncertainties. Phase uncertainties are expressed in percent for comparison. Lines 12 and 13 are tows of the same deployment of 23 instruments but in opposite directions. Differences should include only the effects of uncertainty in the transmitter parameters. Site 52 is a redeployment of the same instrument and its differences should also include uncertainty in instrument rotation and location. Site 39 is the reoccupation of a site by a different receiver, which was towed in an orthogonal direction. Differences for this site add the effects of differences in receiver calibration as well as geologic heterogeneities.

		Amplitude		Phase	
	Range	% Bias	% Difference	% Bias	% Difference
Lines 12 and 13	2–4 km	0.3	2.8	1.3	2.4
	4–6 km	0.6	6.3	1.4	4.1
Site 52	2–4 km	−3.2	1.4	1.3	2.7
	4–6 km	−1.6	4.7	0.5	5.1
Site 39	2–4 km	−2.9	2.4	−0.4	3.2
	4–6 km	−2.6	5.6	0.4	7.1

Comparing the modeled uncertainties to the differences actually observed, we find that our estimates of transmitter parameter uncertainties are approximately correct in amplitude, but too low in phase. In the 2–4 km range, where the observed differences in lines 12 and 13 are from location errors and not random noise, we observe a 2.8% difference in amplitude and a 2.4% (1.4°) difference in phase. We calculate ~2.9% uncertainty in amplitude but only ~1.2% (0.7°) in phase, approximately half what we observe.

Of the components of uncertainty shown, altitude produces some of the largest effects in phase. We based altitude uncertainty on the dip uncertainty because the altitude of the transmitter body is known to centimeter accuracy and the altitude of the center of the dipole is based on its dip. However, this assumes that the seafloor is perfectly flat over the horizontal distance between the altimeter and the center of the dipole. Because the seafloor is not flat, it is possible that the altitude uncertainty is larger than the 3 m we calculated from dip alone.

Table 4. Perturbations used to calculate the effects of uncertainties on the amplitude and phase of electric fields in Figure 18. These values produce phase uncertainties which are lower than calculated from the lines 12–13 comparison. Doubling the altitude perturbation produces values more in line with observations.

Parameter	Perturbation
Receiver orientation	5°
Transmitter dip	1°
Transmitter azimuth	4°
Transmitter altitude	3 m
Inline distance	5 m
Crossline distance	10 m
Finite dipole	250 m

Because we do not know the magnitude of altitude uncertainty due to bathymetry, we make a rough calculation by doubling the contribution calculated from dip. The gray dashed curves shown in Figure 18 are the resulting composite uncertainties if the altitude uncertainty is six meters instead of three. In the 2–4 km range, the amplitude uncertainty is now ~3.3% and the phase uncertainty ~2% (1.1°). Because both values are within a half percent of the observed values, we prefer this increased value of altitude uncertainty and use it in calculations in the remainder of this work.

We repeated this modeling for the four primary frequencies in the survey and show in Figure 19 composite uncertainty curves calculated from the modeled uncertainties added arithmetically, then added in quadrature with instrument noise floors. We have added the finite dipole calculation to the model so that the shortest ranges reflect the influence of the dipole bias. For the noise floors, we used the median S/Ns of all sites in line 13, but this is merely illustrative. Noise varies with instrument, so composite uncertainty curves should be constructed for each instrument using the variances calculated from its data. In the 4–6 km range, the noise from the declining S/N agrees with the variation we observe in the lines 12–13 evaluation (Figure 15c), validating our repeat-tow comparison procedure. We suggest that composite uncertainty curves calculated in this way provide the minimum uncertainty as a function of frequency and range for the Scarborough data set.

We evaluated whether these uncertainties are small enough to allow separate resolution of the gas reservoir and overlying Gearle layer by repeating the presurvey inversion study. In Figure 20, we show the models that result from a standard smooth inversion and a constrained inversion with stabilizing prejudice penalties and breaks in the regularization penalty as described earlier in the text. For both inversions, we used synthetic data in which we applied Gaussian random noise scaled by the curves given in Figure 19. As in the presurvey study, the smooth inversion is unable to separate the signals of the two resistive layers, whereas the constrained inversion is.

There are two differences between these inversions and the fixed-noise-level inversions of the premodel study. First, the resolution to the basement is decreased. All of the presurvey inversion models show an increase in resistivity in accordance with the basement layers. However, those inversions used a fixed noise level at all ranges. As our analysis shows, in real data, the noise increases dramatically with range and in practice this limits the depth-sensitivity of CSEM to shallower depths than a presurvey model study might otherwise indicate. We estimate that the Scarborough CSEM data will not be sensitive to structures over 3 km below the seafloor (4 km bsl).

Second, the resistivity of the Gearle siltstone layer is overestimated in the cut inversions of the presurvey study, but properly estimated here. This suggests that when a fixed error structure is used, the penalty for deviating from the true model is approximately equal across depth. However, when a more realistic error structure is used in which uncertainty increases with

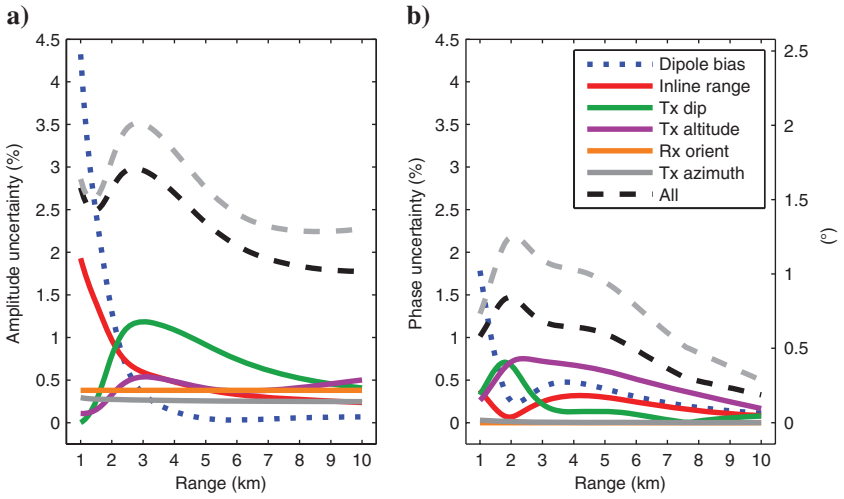

Figure 18. Uncertainty curves in (a) amplitude and (b) phase for the inline electric field calculated by comparing a 1D model of the Scarborough reservoir with a model in which one transmitter parameter is perturbed by the values in Table 4. The dashed black line is a composite uncertainty curve created from all the components added together except the dipole bias (dotted line), which is plotted for reference only. The dashed gray line is the composite uncertainty curve when the uncertainty in altitude is doubled. This more closely matches the phase differences observed in the lines 12 and 13 comparison, but slightly overestimates the amplitude error.

frequency and range, the penalty for deviating from the true model is greater for shallower structure. Resolution decreases with depth faster than idealistic model studies otherwise indicate.

Though 1D inversion of this data set is discussed in detail in the companion paper (Myer, et al., manuscript submitted), for completeness, we present inversion of two sites from line two. Site nine is ~11 km outside of the reservoir boundary and represents the "off reservoir" response, while site 32 is in the middle of the reservoir near where the phase four hydrate line crosses line two. For each site, we inverted the amplitude and phase of the inline data between ±8 km range for four frequencies and using uncertainty curves constructed like those shown in Figure 19 but with the variances calculated for each site. As in the synthetic study, roughness penalties are removed above and below the Gearle and reservoir layers and the inversion is stabilized with resistivity prejudices between 1400 and 2500 m depth.

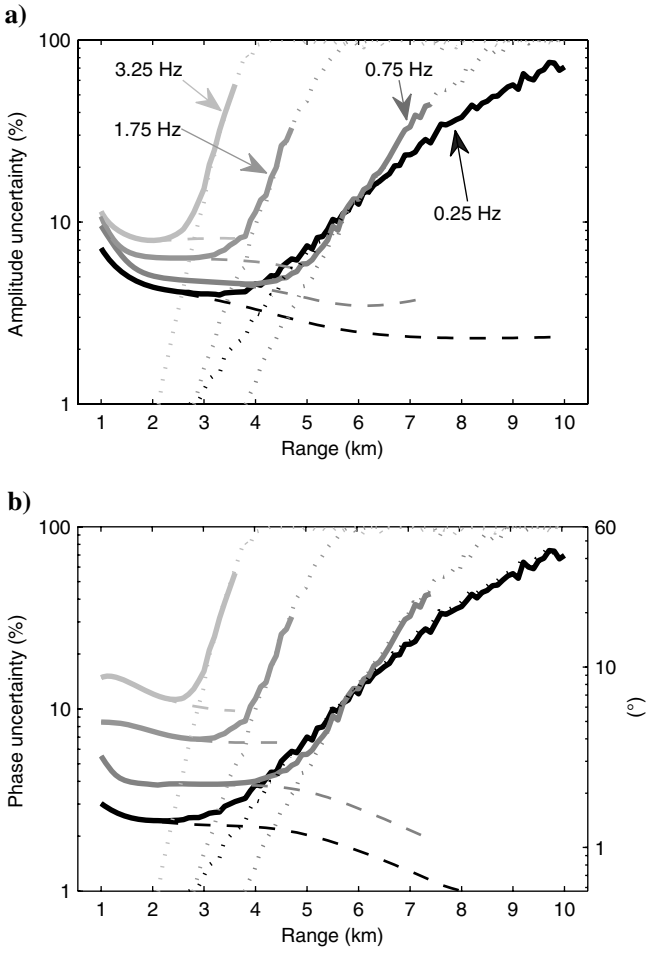

Figure 19. Minimum uncertainty (solid) in (a) amplitude and (b) phase from models and stacking variances added in quadrature. The models (dashed lines) are calculated using a 1D model of the Scarborough reservoir and perturbations in Table 4, but with altitude uncertainties doubled as discussed in the text. Dotted lines are from the median signal-to-noise levels of all sites in line 13 and are illustrative of noise levels which should in practice be derived for each site from its data variance. For a given range and frequency, the solid curve is the minimum uncertainty to use when fitting the data, e.g., in an inversion.

Both sites show enhanced resistivity compared to the off-reservoir geologic background, especially at the Gearle layer (Figure 21). Site nine is far enough outside the reservoir that the enhanced resistivity is unlikely to be low gas saturation and more likely to be resistivity variations in the shallow layers. Site 32 has additional enhanced resistivity from the Gearle down to the gas reservoir layer. The resistivity-thickness product for the top 1.5 km of the model for each site is 611 and 1332 Ωm^2, respectively. The difference is equivalent to a 29 m × 25 Ωm resistor, which is the approximate dimension of the main body of the reservoir, and is concentrated primarily at the depth of the reservoir layer. The synthetic results predicted that the inversion would be unable to completely concentrate the anomaly at the reservoir layer, which does seem to be the case for these two sites.

These two inversions are fit to rms 1.3 and 1.7, respectively, and a large portion of this misfit is from the disparity between the in-tow and out-tow data. This is typical of variations in geology along the tow line. If the data are separately inverted as in-tow only and out-tow only, then rms 1.0 is easily reached in each case and the resulting models are only slightly different from the models in Figure 21.

It is interesting to note that the on- and off-reservoir sites have overestimated the resistivity of the Gearle siltstone layer by the same amount. Although from synthetic models, we expect some "cross-talk" between the Gearle and reservoir layers (c.f. Figure 4b), it is surprising that it occurs to such a degree in the off-reservoir site in which there is no reservoir. This raises the possibility of significant anisotropy in the Gearle layer. The estimates of resistivity shown in Figure 2 are derived from well logs, which measure horizontal resistivity, but as a siltstone, the Gearle is likely to have

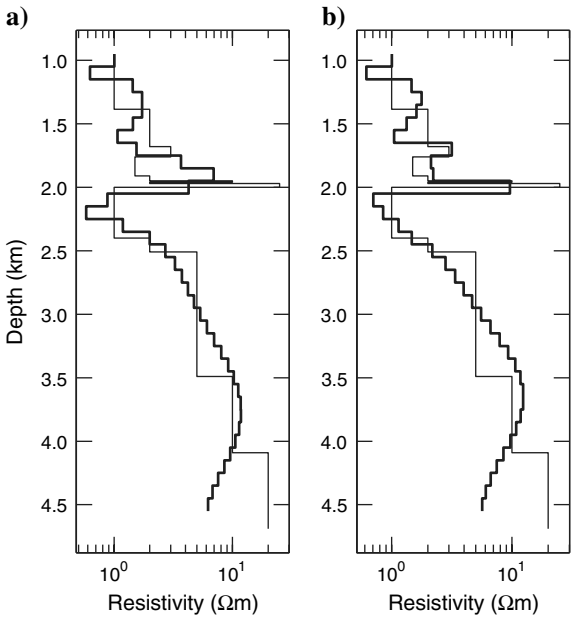

Figure 20. 1D inversion results for the 2D synthetic model data of the Scarborough reservoir (thin line), with uncertainties and Gaussian random noise scaled by the curves in Figure 19. The roughness penalty of the standard Occam inversion (a) smooths the Gearle and reservoir signals together. When preferences and breaks in the roughness penalty as described in Figure 4b are introduced (b), the inversion resolves separate resistive layers of approximately correct resistivity thickness product.

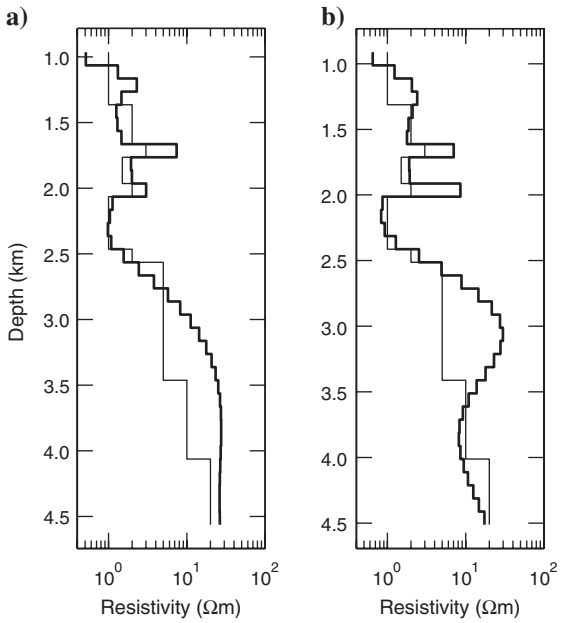

Figure 21. 1D inversion results for two sites on line two. Site nine (a) is 11 km outside the reservoir boundary and site 32 (b) is near the center of it. The thin line is the off-reservoir geologic background model. For both inversions, cuts and prejudices were applied as described in Figure 4b. The off and on reservoir require resistivities above the background model. The resistivity-thickness product for the top 1.5 km of each site is 611 and 1332 Ωm^2, respectively. The difference is equivalent to a 29 m × 25 Ωm resistor, which is the approximate dimension of the main body of the reservoir.

increased vertical resistivity compared to its horizontal resistivity. The CSEM inversion, which is sensitive to vertical and horizontal resistivity, is indicating an increased vertical resistivity over our background model (7 Ωm compared to 3 Ωm).

CONCLUSIONS

We have discussed the 2009 CSEM survey over the Scarborough gas field and shown that recent improvements in transmitter navigation and data processing techniques yield high-quality data with predicted uncertainties of just a few percent at close ranges. Forward modeling of the predicted uncertainties in the transmitter parameters, along with bias in the finite dipole size, yields an error estimate that is not equal in amplitude and phase, suggesting that inversion in this basis is more desirable than in the complex basis (i.e., real and imaginary). Also, we show that uncertainties calculated this way can at times be too conservative.

We demonstrate that more accurate uncertainties can be calculated by towing the same line of receivers twice in opposite directions. Comparing the residuals for each line yields a Gaussian distribution that is directly related to the aggregate uncertainty of the transmitter parameters. For Scarborough, this is 2.8% in amplitude and 2.4% (1.4°) in phase between 2 and 4 km range and grows at longer ranges due to the decrease in the S/N. We further show that perturbation analysis of the repeat tow line data allows constraints to be placed on systematic error in the transmitter inline location and dip. For this survey, these values are ±5 m and ±1°, respectively.

Initial 1D inversions with the improved error model are in good agreement with the resistivity profile determined by well logs. However, there is an indication that the vertical resistivity of the Gearle siltstone may be at least a factor of two above the measured horizontal resistivity.

ACKNOWLEDGMENTS

The authors are grateful to BHP Billiton Petroleum for funding this project in its entirety and for providing the background information we needed for the experimental design phase. The captain, crew, and scientific party of the R/V Roger Revelle worked hard to make this project a success, and we thank them all. We thank Graeme Cairns and two anonymous reviewers for their helpful suggestions. We thank Brent Wheelock for his improvements to the instrument calibrations, which have helped us to obtain such high accuracy in our data. We also thank BHP Billiton, Shell, Esso Australia, and Chevron for providing ingress permissions for this survey. More information and data can be found at http://marineemlab.ucsd.edu/Projects/Scarborough.

REFERENCES

Boyd, R., P. E. Williamson, and B. U. Haq, 1992, Seismic stratigraphy and passive margin evolution of the southern Exmouth Plateau, *in* U. Von Rad, and B. U. Haq, eds., Proceedings of the ODP, Science Results: Ocean Drilling Program.

Constable, S., 2010, Ten years of marine CSEM for hydrocarbon exploration: Geophysics, **75**, no. 5, 75A67–75A81, doi: 10.1190/1.3483451.

Constable, S., and C. S. Cox, 1996, Marine controlled-source electromagnetic sounding: Part 2. The PEGASUS experiment: Journal of Geophysical Research Solid Earth: JGR, **101**, no. B3, 5519–5530, doi: 10.1029/95JB03738.

Constable, S., A. S. Orange, G. M. Hoversten, and H. F. Morrison, 1998, Marine magnetotellurics for petroleum exploration, Part I: A sea-floor equipment system: Geophysics, **63**, 816–825, doi: 10.1190/1.1444393.

Constable, S., and C. J. Weiss, 2006, Mapping thin resistors and hydrocarbons with marine EM methods: Insights from 1D modeling: Geophysics, **71**, no. 6, G43–G51, doi: 10.1190/1.2187748.

Cox, C. S., S. C. Constable, A. D. Chave, and S. C. Webb, 1986, Controlled-source electromagnetic sounding of the oceanic lithosphere: Nature, **320**, no. 6057, 52–54, doi: 10.1038/320052a0.

Driscoll, N. W., and G. D. Karner, 1998, Lower crustal extension across the northern Carnarvon basin, Australia: Evidence for an eastward dipping detachment: Journal of Geophysical Research Solid Earth, **103**, no. B3, 4975–4991, doi: 10.1029/97JB03295.

Edwards, N., 2005, Marine controlled-source electromagnetics: Principles, methodologies, future commercial applications: Surveys in Geophysics, **26**, 675–700, doi: 10.1007/s10712-005-1830-3.

Ellingsrud, S., T. Eidesmo, S. Johansen, M. C. Sinha, L. M. MacGregor, and S. Constable, 2002, Remote sensing of hydrocarbon layers by seabed logging (SBL): Results from a cruise offshore Angola: The Leading Edge, **21**, 972–982, doi: 10.1190/1.1518433.

Exon, N. F., U. Von Rad, and U. Von Stackelberg, 1982, The geological development of the passive margins of the Exmouth Plateau off northwest Australia: Marine Geology, **47**, no. 1–2, 131–152, doi: 10.1016/0025-3227(82)90023-8.

Haq, B. U., R. L. Boyd, N. F. Exon, and U. Von Rad, 1992, Evolution of the central Exmouth Plateau; a post-drilling perspective, *in* U. Von Rad, and B. U. Haq, eds., Proceedings of the ODP, Science Results: Ocean Drilling Program.

Keisler, S. R., and R. H. Rhyne, 1976, An assessment of prewhitening in estimating power spectra of atmospheric turbulence at long wavelengths: NASA Langley Research Center.

Key, K., 2009, 1D inversion of multicomponent, multifrequency marine CSEM data: Methodology and synthetic studies for resolving thin resistive layers: Geophysics, **74**, no. 2, F9–F20, doi: 10.1190/1.3058434.

Key, K., 2012, Marine electromagnetic studies of seafloor resources and tectonics: Surveys in Geophysics, **33**, no. 1, 135–167, doi: 10.1007/s10712-011-9139-x.

Key, K., and A. Lockwood, 2010, Determining the orientation of marine CSEM receivers using orthogonal Procrustes rotation analysis: Geophysics, **75**, no. 3, F63–F70, doi: 10.1190/1.3378765.

Key, K., and J. Ovall, 2011, A parallel goal-oriented adaptive finite element method for 2.5-D electromagnetic modeling: Geophysical Journal International, **186**, 137–154, doi: 10.1111/gji.2011.186.issue-1.

Leroy, C. C., and F. Parthiot, 1998, Depth-pressure relationships in the oceans and seas: The Journal of the Acoustical Society of America, **103**, no. 3, 1346–1352, doi: 10.1121/1.421275.

Lim, K., G. Ivey, and R. Nokes, 2008, The generation of internal waves by tidal flow over continental shelf/slope topography: Environmental Fluid Mechanics, **8**, no. 5–6, 511–526, doi: 10.1007/s10652-008-9085-4.

Lorenzo, J. M., J. C. Mutter, and R. L. Larson, 1991, Development of the continent-ocean transform boundary of the southern exmouth plateau: Geology, **19**, 843–846, doi: 10.1130/0091-7613(1991)019<0843:DOTCOT>2.3.CO;2.

MacGregor, L., M. Sinha, and S. Constable, 2001, Electrical resistivity structure of the Valu Fa Ridge, Lau Basin, from marine controlled-source electromagnetic sounding: Geophysical Journal International, **146**, 217–236, doi: 10.1046/j.1365-246X.2001.00440.x.

Mutter, J. C., and R. L. Larson, 1989, Extension of the Exmouth Plateau, offshore northwestern Australia: Deep seismic reflection/refraction evidence for simple and pure shear mechanisms: Geology, **17**, 15–18, doi: 10.1130/0091-7613(1989)017<0015:EOTEPO>2.3.CO;2.

Myer, D., S. Constable, and K. Key, 2010, A marine EM survey of the Scarborough gas field, northwest shelf of Australia: First Break, **28**, 77–82.

Myer, D., S. Constable, and K. Key, 2011, Broad-band waveforms and robust processing for marine CSEM surveys: Geophysical Journal International, **184**, 689–698, doi: 10.1111/gji.2011.184.issue-2.

Newman, G. A., M. Commer, and J. J. Carazzone, 2010, Imaging CSEM data in the presence of electrical anisotropy: Geophysics, **75**, no. 2, F51–F61, doi: 10.1190/1.3295883.

Orange, A., K. Key, and S. Constable, 2009, The feasibility of reservoir monitoring using time-lapse marine CSEM: Geophysics, **74**, no. 2, F21–F29, doi: 10.1190/1.3059600.

Shumway, R. H., and D. S. Stoffer, 2000, Time series analysis and its applications, 1st ed.: Springer Verlag.

Sinha, M. C., P. D. Patel, M. J. Unsworth, T. R. E. Owen, and M. R. G. Maccormack, 1990, An active source electromagnetic sounding system for marine use: Marine Geophysical Researches, **12**, 59–68, doi: 10.1007/BF00310563.

Van Gastel, P., G. N. Ivey, M. J. Meuleners, J. P. Antenucci, and O. Fringer, 2009, The variability of the large-amplitude internal wavefield on the Australian northwest shelf: Continental Shelf Research, **29**, no. 11–12, 1373–1383, doi: 10.1016/j.csr.2009.02.006.

Veevers, J. J., and M. H. Johnstone, 1974, Comparative stratigraphy and structure of the western Australian margin and the adjacent deep ocean floor: Initial Reports of the DSDP, **27**, 571–585, doi: 10.2973/dsdp.proc.27.129.1974.

Webb, S., and C. S. Cox, 1984, Pressure and electric fluctuations on the deep seafloor: Background noise for seismic detection: Geophysical Research Letters, **11**, 967–970, doi: 10.1029/GL011i010p00967.

Webb, S. C., and S. C. Constable, 1986, Microseism propagation between twosites on the deep seafloor: Bulletin of the Seismological Society of America, **76**, 1433–1445.

Webb, S. C., S. C. Constable, C. S. Cox, and T. K. Deaton, 1985, A sea-floor electric-field instrument: Journal of Geomagnetism and Geoelectricity, **37**, no. 12, 1115–1129, doi: 10.5636/jgg.37.1115.

Webb, S. C., and C. S. Cox, 1986, Observations and modeling of seafloor microseisms: Journal of Geophysical Research, **91**, 7343–7358, doi: 10.1029/JB091iB07p07343.

Zhdanov, M. S., 2010, Electromagnetic geophysics: Notes from the past and the road ahead: Geophysics, **75**, no. 5, 75A49–75A66, doi: 10.1190/1.3483901.